Constrained Control of Low-Capacitance Delta Cascaded H-Bridge StatComs: A Model Predictive Control Approach

Ezequiel Rodriguez, *Student Member, IEEE*, Ramon Leyva, *Senior Member, IEEE*, Christopher D. Townsend, *Member, IEEE*, Glen G. Farivar, *Senior Member, IEEE*, Hossein Dehghani Tafti, *Senior Member, IEEE*, and Josep Pou, *Fellow, IEEE*

***Abstract*—This article presents a constrained model predictive control (MPC) strategy for a three-phase low-capacitance static compensator (LC-StatCom) with delta configuration. The controller consists of an outer loop that provides dynamic references for the active grid current component and the circulating current; whereas, the inner predictive loop minimizes the quadratic error of state variables subject to operating limit conditions, thus providing optimal control signals that produce a fast response while guaranteeing the prescribed safe operating limit conditions. The article also proposes an enhanced discrete-time model, which uses intersample values, that improves the accuracy of the model predictions when the sampling rate is not high enough to assume constant state variables. As a result, it facilitates the implementation of MPC on less powerful processors compared to the conventional modeling. The proposed control is especially suited for the LC-StatComs since it incorporates analytical computation of desired steady-state trajectories, which takes into account the induced oscillation on the capacitor voltages that are inherent to the LC-StatComs. The proposed approach has been verified by simulation and experimentally with a laboratory prototype.**

***Index Terms*—Bilinear system control, cascaded H-bridge (CHB), model predictive control (MPC), multilevel converter, predictive models, static compensator (STATCOM).**

Manuscript received December 6, 2020; revised February 3, 2021 and March 30, 2021; accepted May 19, 2021. Date of publication June 1, 2021; date of current version August 16, 2021. This work was supported by the Singapore Ministry of Education Academic Research Fund Tier 1 under Grant 2017-T1-001-213 (RG 90/17) and in part by the NTU Start-up under Grant 000603-00001 (Compact, and Reliable Power Converters). Recommended for publication by Associate Editor D. M. Xu. *(Corresponding author: Ezequiel Rodriguez.)*

Ezequiel Rodriguez and Josep Pou are with the School of Electrical and Electronic Engineering, Nanyang Technological University, Singapore 639798, Singapore (e-mail: ezequiel001@e.ntu.edu.sg; josep.pou@ieee.org).

Ramon Leyva is with the Departament d'Enginyeria Electrónica, Eléctrica i Automática, Universitat Rovira i Virgili, 43007 Tarragona, Spain (e-mail: ramon.leyva@urv.cat).

Christopher D. Townsend and Hossein Dehghani Tafti are with the Department of Electrical, Electronic and Computer Engineering, University of Western Australia, Crawley, WA 6009, Australia (e-mail: townsend@ieee.org; hossein002@e.ntu.edu.sg).

Glen G. Farivar is with the Energy Research Institute, Nanyang Technological University, Singapore 639798, Singapore (e-mail: gh_farivar@hotmail.com).

Color versions of one or more figures in this article are available at https://doi.org/10.1109/TPEL.2021.3085880.

Digital Object Identifier 10.1109/TPEL.2021.3085880

I. Introduction

THE low-capacitance static compensator (LC-StatCom[1]) based on the cascaded H-bridge (CHB) multilevel converter [1]–[7] has been recently proposed as an alternative to reduce capacitance values and, thus, the converter size and cost. Nevertheless, the reduced capacitance, and thus low energy stored in the converter, inflicts the LC-StatCom with: 1) a large magnitude low-frequency voltage oscillation, and 2) a nonnegligible coupling between the capacitor voltage dynamics and the inductor current dynamics. These particularities make the LC-StatCom control challenging.

Some early work on the control design of the LC-StatCom was presented in [1], [2], and[8], where the main objective was to increase the control effectiveness by using analytic feedforward filtering techniques to substitute the conventional low-pass filter that reduces the response bandwidth. The design and control of an LC-StatCom were also discussed in [9] and [10], where a second-order generalized integrator was used to estimate the maximum capacitor voltage. A multi-input linear control law, based on incremental passivity theory, that ensures large-signal stability was used to control the LC-StatCom in [11]. This method achieved a fast dynamic, but, as for the rest of the aforementioned references, the focus was to address the control problems within a phase; hence, a single-phase LC-StatCom was used for demonstration.

With regard to the three-phase LC-StatComs, [7],[12], and[13] are worth highlighting, where the use of third-harmonic zero-sequence to achieve improved performance of the LC-StatComs is discussed. Particularly, [7] and [13] cover, in detail, the restricted region of operation in inductive mode. However, achieving fast response and constraining the state variables during transients was overlooked.

Compared to the LC-StatCom, the control of conventional StatComs is a much more comprehensively studied field [14]–[18]. In this regard, cascade approach is one of the established popular control options. The inner current control loop can be based on voltage oriented control, as in the previous references, or using proportional plus resonant current

[1]Note that the LC acronym in LC-StatCom refers to low-capacitance and not to the widely used LC filter.

controllers, as in [9]. The outer control loop regulates and balances the capacitor voltages by modifying the references used in the inner current control loop. This represents a common approach to compensate converter parametric uncertainties. However, none of these control schemes enforces a limitation on the capacitor voltages during the transient operation.

In the LC-StatComs, due to the large induced capacitor voltage oscillations, it is important to limit the capacitor voltages within a predefined range. Thus, there is a need for a three-phase LC-StatCom control strategy that considers the particularities of the LC-StatCom and delivers a fast dynamic while confining the sate variables, i.e., the capacitor voltages and the inductor currents, in safe operating regions.

Model predictive control (MPC) is an attractive way to deal with operating limit conditions [19], [20]. Several authors have studied the MPC application for StatCom control [21]–[24]. In [21], a partially stratified MPC approach (current and capacitor voltage control solved sequentially) is applied to a StatCom with star configuration. In [22] and [23], the MPC formulation concerns with modulation-related problems, resulting in high-quality voltages at relatively low switching frequencies. A heuristic MPC approach is analyzed in [22] for a StatCom with star configuration, whereas an optimal pulse pattern MPC technique is analyzed in [23] for a StatCom with delta configuration. A fault detection and localization algorithm based on MPC is proposed in [24] for a single-phase CHB. All the aforementioned MPC contributions consider a conventional StatCom. Adapting these techniques to the particularities of LC-StatComs is a contribution of this article. This article describes the design of a constrained control approach, based on the MPC, for the LC-StatComs. Adapting the MPC to the LC-StatCom requires taking into account the following new considerations:

1) design of an outer control loop that properly handles converter parametric uncertainty by using the nonconstant capacitor energies;
2) due to the reduced capacitor size in the LC-StatComs, the bilinear terms of their dynamics should be taken into account;
3) modeling and inclusion of the capacitor voltage constraints in the underlying optimization problem so that safe operating conditions are guaranteed during transients;
4) due to the reduced capacitor size, the low-frequency voltage oscillation on the capacitors is not negligible and, therefore, must be taken into account when designing the system references (state variables and control signals at equilibrium trajectory);
5) choosing an optimization algorithm that minimizes computational burden and facilitates real-time digital control.

Addressing the above considerations, the article proposes a scheme based on the common cascade loop structure [15], where voltage and current magnitudes are constrained using an MPC approach. In the MPC approach, the calculation of the prediction errors takes into account the desired state trajectory in transient and steady-state operation. In steady-state operation, trajectories are calculated according to the converter model, as in [11]. Transients in the desired state trajectory consider uncertainty according to [14], whereas the calculation of the prediction errors takes into account the bilinear nature of the converter. Also, an optimization algorithm with low iteration cost based on the alternating direction method of multipliers (ADMM) has been chosen to do the experimental implementation.

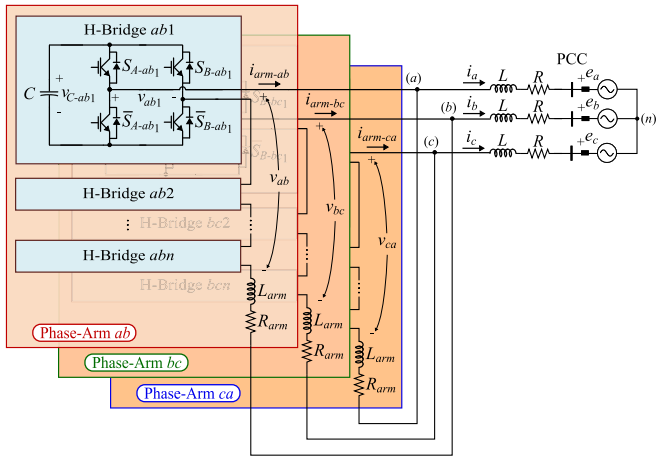

Fig. 1. Circuit diagram of the LC-StatCom with delta configuration.

The article is organized as follows. Section II describes the modeling of the LC-StatCom with delta configuration, where the discrete-time model is derived. The section also reviews the common Euler approximation model and proposes a new one that does not neglect the bilinear terms. Based on the model, the proposed constrained MPC is described in detail in Section III, in which the state trajectory, constraints modeling, and the resultant optimization problem are specifically addressed. Section IV provides experimental results to corroborate the performance of the proposed approach. In addition, complimentary simulation results, which show multilevel waveforms, are presented in Section V. Section VI summarizes the conclusion of the article.

II. LC-StatCom With Delta Configuration

This section reviews the topology of the LC-StatCom with delta configuration, its state variables, and its state-space model. Then, the averaged model of the system is derived and, subsequently, discretized. The discretized model is used in the proposed constrained MPC, which is explained in the next section.

A. Topology

The converter topology is shown in Fig. 1. The power converter consists of three identical phase-arms $x \in \mathcal{X} = \{ab, bc, ca\}$ with delta configuration. Each phase-arm includes n series-connected H-bridges $j \in \mathcal{J} = \{1, 2, \ldots, n\}$ and an arm inductor L_{arm}. Each H-bridge consists of a floating capacitor C at its dc side and two pairs of power switches that work in a complementary manner, which allows the generation of three different output voltage levels. The three ac terminals of the power converter (a), (b), (c) are connected to the point of common coupling (PCC) grid voltages e_a, e_b, e_c through the filtering inductors L. Losses are also modeled with the series resistances R and R_{arm}, as depicted in Fig. 1.

B. CHB Multilevel Converter Modeling

In the CHB multilevel converter with n series-connected H-bridges per phase-arm, shown in Fig. 1, each converter voltage v_x is the sum of the individual H-bridge ac voltages, i.e., $v_x = \sum_{j\in\mathcal{J}} v_{xj}$. The ac and dc sides of the converter, in the jth H-bridge for the xth phase-arm, are related by the discontinuous control function S_{xj} as

$$\begin{aligned} v_{xj} &= S_{xj} v_{C-xj} \\ C\frac{d}{dt} v_{C-xj} &= -S_{xj} i_{\text{arm}-x} \end{aligned} \tag{1}$$

where v_{C-xj} is the capacitor voltage. Note that it has been considered that all the H-bridges have the same nominal capacitance value C.

The discrete term $S_{xj} = S_{A-xj} - S_{B-xj}$ belongs to the finite set $\{-1,\ 0,\ 1\}$, where $S_{A-xj},\ S_{B-xj} \in \{0,\ 1\}$ corresponds to the switching states of the top switches (according to Fig. 1).

The phase-arm converter voltages v_{ab}, v_{bc}, v_{ca} can be related to their corresponding cluster voltages (sum-capacitor voltages), i.e., $v_{\Sigma-ab} = \sum_{j\in\mathcal{J}} v_{C-abj}$ for the phase-arm ab, and similarly for arms bc and ca, as

$$v_x = S_x v_{\Sigma-x} \tag{2}$$

where the equivalent switching function S_x corresponds to

$$S_x = \frac{1}{n}\sum_{j\in\mathcal{J}} S_{xj} \in \left\{-1,\ \frac{-n+1}{n},\ \ldots\ 0\ \ldots,\ \frac{n-1}{n},\ 1\right\}. \tag{3}$$

Note that this assumes that the capacitor voltages are balanced within the converter phase-arm ($v_{C-xj} = v_{\Sigma-x}/n, \forall j,\ x$). This implies that an interbridge balancing algorithm is implemented within the control in order to fulfill this assumption [14].

Similarly, the arm currents $i_{\text{arm}-ab}$, $i_{\text{arm}-bc}$, $i_{\text{arm}-ca}$ can be related to their corresponding cluster voltage variations as

$$\frac{C}{n}\frac{d}{dt} v_{\Sigma-x} = -S_x i_{\text{arm}-x} \tag{4}$$

which governs the cluster voltage dynamics.

Inductor current dynamics are determined by applying Kirchhoff's voltage law in the circuit shown in Fig. 1. The details to derive the differential equations that define the current dynamics are provided in the Appendix.

C. Bilinear Continuous-Time Averaged Model

The number of levels of the equivalent switching functions S_{ab}, S_{bc}, S_{ca}, which can be generated due to the switching nature of the converter, is finite, as (3) indicates. The equivalent switching functions in (3) can be approximated by their averaged values over a switching period; thus the modulation signals δ_{ab}, δ_{bc}, δ_{ca} correspond to

$$\delta_x = \frac{1}{T_{\text{sw}}}\int_{t-T_{\text{sw}}}^{t} S_x dt \in [-1,\ 1]. \tag{5}$$

The switching period T_{sw} is assumed much (at least 10 times) shorter than the converter system time constants.

Then, the ac and dc sides of the converter in the averaged model are related by the continuous modulation function δ_x. The variables of the model are considered henceforth to be averaged variables. For the purpose of simplicity, no difference in notation between the averaged and exact variables has been included.

The dynamic behavior of the CHB converter uses as state variables the grid currents i_a and i_b, together with the circulating current i_{circ}, and the cluster voltages $v_{\Sigma-ab}$, $v_{\Sigma-bc}$, $v_{\Sigma-ca}$; the control inputs in the model correspond to the modulation signals δ_{ab}, δ_{bc}, δ_{ca}. The state variables are grouped in the vector $\boldsymbol{x} \in \mathbb{R}^6$, the control inputs are grouped in the vector $\boldsymbol{u} \in \mathbb{R}^3$, and the PCC grid voltages are grouped in the vector $\boldsymbol{e} \in \mathbb{R}^3$ as

$$\begin{aligned} \boldsymbol{x} &= [i_a\ i_b\ i_{\text{circ}}\ v_{\Sigma-ab}\ v_{\Sigma-bc}\ v_{\Sigma-ca}]^T \\ \boldsymbol{u} &= [\delta_{ab}\ \delta_{bc}\ \delta_{ca}]^T \\ \boldsymbol{e} &= [e_a\ e_b\ e_c]^T. \end{aligned} \tag{6}$$

Using (4) and (85), the following nonlinear state-space model with continuous variables is obtained:

$$\dot{\boldsymbol{x}} = \boldsymbol{A}\boldsymbol{x} + \boldsymbol{B}(\boldsymbol{x})\,\boldsymbol{u} + \boldsymbol{W}\boldsymbol{e} \tag{7}$$

where the system matrix $\boldsymbol{A}$, input matrix $\boldsymbol{B}(\boldsymbol{x})$, and matrix $\boldsymbol{W}$ correspond to

$$\boldsymbol{A} = \begin{bmatrix} \boldsymbol{A}_{11} & \boldsymbol{0}_{3\times3} \\ \boldsymbol{0}_{3\times3} & \boldsymbol{0}_{3\times3} \end{bmatrix} \tag{8}$$

$$\boldsymbol{B}(\boldsymbol{x}) = \begin{bmatrix} \boldsymbol{b}_1(\boldsymbol{x}) & \boldsymbol{b}_2(\boldsymbol{x}) & \boldsymbol{b}_3(\boldsymbol{x}) \end{bmatrix} \tag{9}$$

$$\boldsymbol{W} = -\frac{1}{3L_{eq}}\begin{bmatrix} 2 & -1 & -1 \\ -1 & 2 & -1 \\ 0 & 0 & 0 \\ 0 & 0 & 0 \\ 0 & 0 & 0 \\ 0 & 0 & 0 \end{bmatrix} \tag{10}$$

with

$$\boldsymbol{A}_{11} = \begin{bmatrix} -\frac{R_{\text{eq}}}{L_{\text{eq}}} & 0 & 0 \\ 0 & -\frac{R_{\text{eq}}}{L_{\text{eq}}} & 0 \\ 0 & 0 & -\frac{R_{\text{arm}}}{L_{\text{arm}}} \end{bmatrix} \tag{11}$$

$$\boldsymbol{b}_1(\boldsymbol{x}) = \begin{bmatrix} \frac{1}{3L_{\text{eq}}} v_{\Sigma-ab} \\ -\frac{1}{3L_{\text{eq}}} v_{\Sigma-ab} \\ \frac{1}{3L_{\text{arm}}} v_{\Sigma-ab} \\ -\frac{1}{3C/n}\left(i_a - i_b + 3i_{\text{circ}}\right) \\ 0 \\ 0 \end{bmatrix} \tag{12}$$

$$\boldsymbol{b}_2(\boldsymbol{x}) = \begin{bmatrix} 0 \\ \frac{1}{3L_{\text{eq}}} v_{\Sigma-bc} \\ \frac{1}{3L_{\text{arm}}} v_{\Sigma-bc} \\ 0 \\ -\frac{1}{3C/n}\left(i_a + 2i_b + 3i_{\text{circ}}\right) \\ 0 \end{bmatrix} \tag{13}$$

$$\boldsymbol{b}_3(\boldsymbol{x}) = \begin{bmatrix} -\frac{1}{3L_{\text{eq}}} v_{\Sigma-ca} \\ 0 \\ \frac{1}{3L_{\text{arm}}} v_{\Sigma-ca} \\ 0 \\ 0 \\ -\frac{1}{3C/n}\left(-2i_a - i_b + 3i_{\text{circ}}\right) \end{bmatrix}. \tag{14}$$

Note that the terms of $\boldsymbol{B}(\boldsymbol{x})$ depend linearly on the state $\boldsymbol{x}$, and $\boldsymbol{B}(\boldsymbol{x})$ is multiplied by the control vector $\boldsymbol{u}$, thus showing a bilinear nature of (7).

D. Discrete-Time Averaged Model

Because of the discrete-time implementation of the MPC controller, a discrete-time representation of the model in (7) is needed.

Assuming that the state $\boldsymbol{x}$, the input $\boldsymbol{u}$, and the voltage $\boldsymbol{e}$ are approximately constant between the sampling instants k and $k+1$, the discrete-time model corresponds to

$$\boldsymbol{x}(k+1) = \boldsymbol{A}'_d \boldsymbol{x}(k) + \boldsymbol{B}'_d(\boldsymbol{x}(k))\,\boldsymbol{u}(k) + \boldsymbol{W}'_d \boldsymbol{e}(k) \tag{15}$$

with matrices

$$\begin{aligned} \boldsymbol{A}'_d &= e^{\boldsymbol{A}T_s} \\ \boldsymbol{B}'_d(\boldsymbol{x}(k)) &= \left(\int_{\tau=0}^{T_s} e^{\boldsymbol{A}\tau} d\tau\right) \boldsymbol{B}(\boldsymbol{x}(k)) \\ \boldsymbol{W}'_d &= \left(\int_{\tau=0}^{T_s} e^{\boldsymbol{A}\tau} d\tau\right) \boldsymbol{W} \end{aligned} \tag{16}$$

which can be simplified, for short enough sampling periods T_s, assuming the Euler's method, i.e., $e^{\boldsymbol{A}T_s} \approx \boldsymbol{I} + \boldsymbol{A}T_s$. Note that in (16), the matrix $\boldsymbol{B}(\boldsymbol{x})$ has been removed from the integral sign as it is assumed constant between k and $k+1$. If the sampling period T_s is long enough, the variations of state $\boldsymbol{x}$ along the sampling period could be nonnegligible, and, thus, it is not appropriate to consider $\boldsymbol{B}(\boldsymbol{x})$ with a constant value of $\boldsymbol{x}$ equal to the value sampled at the beginning of the period $\boldsymbol{x}(k)$. Therefore, the models (15) and (16) demand high sampling rates. As an alternative to using high sampling rates, enhanced dynamic models could accurately predict state variables for longer sampling periods.

Not assuming that the state $\boldsymbol{x}$ and the voltage $\boldsymbol{e}$ are constant between the sampling instants k and $k+1$ implies that the terms $\boldsymbol{B}(\boldsymbol{x})$ and $\boldsymbol{W}\boldsymbol{e}$ in (7) vary between the instants k and $k+1$ [25], thus resulting in a more accurate model (17), involving the calculation of integrals $\int_{\tau=0}^{T_s} e^{\boldsymbol{A}\tau}\boldsymbol{B}(\boldsymbol{x}(\tau))d\tau$ and $\int_{\tau=0}^{T_s} e^{\boldsymbol{A}\tau}\boldsymbol{W}\boldsymbol{e}(\tau)d\tau$

$$\boldsymbol{x}(k+1) = \boldsymbol{A}_d \boldsymbol{x}(k) + \boldsymbol{B}_d(\boldsymbol{x}(k))\,\boldsymbol{u}(k) + \boldsymbol{w}_d(k) \tag{17}$$

with

$$\begin{aligned} \boldsymbol{A}_d &= e^{\boldsymbol{A}T_s} \\ \boldsymbol{B}_d(\boldsymbol{x}(k)) &= \int_{\tau=0}^{T_s} e^{\boldsymbol{A}\tau}\boldsymbol{B}(\boldsymbol{x}(\tau))\,d\tau \\ \boldsymbol{w}_d(k) &= \int_{\tau=0}^{T_s} e^{\boldsymbol{A}\tau}\boldsymbol{W}\boldsymbol{e}(\tau)\,d\tau. \end{aligned} \tag{18}$$

The aforementioned integrals can be evaluated in M equal subintervals, which considers the evolution of the state $\boldsymbol{x}$ and the voltage $\boldsymbol{e}$ inside the sampling period T_s. Therefore, (17) and (18) can be simplified by the following accurate discrete-time model that uses intersample values:

$$\boldsymbol{x}(k+1) = \boldsymbol{A}_d \boldsymbol{x}(k) + \boldsymbol{B}_d(\boldsymbol{x}(k))\,\boldsymbol{u}(k) + \boldsymbol{W}_d \boldsymbol{e}(k) \tag{19}$$

with

$$\begin{aligned} \boldsymbol{A}_d &= \left(\boldsymbol{I} + \frac{T_s}{M}\boldsymbol{A}\right)^M \\ \boldsymbol{B}_d(\boldsymbol{x}(k)) &= \\ &\frac{T_s}{M}\sum_{m=0}^{M-1}\left(\boldsymbol{I} + \frac{T_s}{M}\boldsymbol{A}\right)^{M-1-m} \boldsymbol{B}\left(\boldsymbol{x}\left(k + m\frac{T_s}{M}\right)\right) \\ \boldsymbol{W}_d &= \frac{T_s}{M}\sum_{m=0}^{M-1}\left(\boldsymbol{I} + \frac{T_s}{M}\boldsymbol{A}\right)^{M-1-m} \boldsymbol{W}\boldsymbol{R}_\omega^m \end{aligned} \tag{20}$$

where $\boldsymbol{x}(k + m\frac{T_s}{M})$ is the value of the state inside the sampling period T_s, and the matrix $\boldsymbol{R}_\omega$ represents a rotation during a time T_s/M, i.e.,

$$\boldsymbol{R}_\omega = \boldsymbol{T}^{\dagger}_{\alpha\beta} \begin{bmatrix} \cos\left(\omega\frac{T_s}{M}\right) & -\sin\left(\omega\frac{T_s}{M}\right) \\ \sin\left(\omega\frac{T_s}{M}\right) & \cos\left(\omega\frac{T_s}{M}\right) \end{bmatrix} \boldsymbol{T}_{\alpha\beta}. \tag{21}$$

Note that matrices $\boldsymbol{T}_{\alpha\beta}$ and $\boldsymbol{T}^{\dagger}_{\alpha\beta}$ correspond to the reduced power conservative Clarke transformation and its pseudoinverse (inverse matrix), respectively, i.e.,

$$\begin{aligned} \boldsymbol{T}_{\alpha\beta} &= \sqrt{\tfrac{2}{3}} \begin{bmatrix} 1 & -\frac{1}{2} & -\frac{1}{2} \\ 0 & \frac{\sqrt{3}}{2} & -\frac{\sqrt{3}}{2} \end{bmatrix} \\ \boldsymbol{T}^{\dagger}_{\alpha\beta} &= \sqrt{\tfrac{2}{3}} \begin{bmatrix} 1 & 0 \\ -\frac{1}{2} & \frac{\sqrt{3}}{2} \\ -\frac{1}{2} & -\frac{\sqrt{3}}{2} \end{bmatrix}. \end{aligned} \tag{22}$$

Having a good prediction of the state at each instant when the MPC actuates is very important, and this depends on the value of M.

Next, as an illustration, it is shown how the state predictions improve when the proposed intersample models (19) and (20) are used. Particularly, in Fig. 2, the accuracy of the proposed predictors (19) and (20) with $M = 10$ intersamples (right plots) is evaluated and compared with the common approach in (15) and (16) (left plots), when a sudden change in the instantaneous reactive power reference occurs.

Fig. 2 corroborates, when the sampling frequency is 2500 Hz, that both in steady-state and transient operation, the prediction errors are significantly smaller when the bilinear terms are treated as the proposed approach does. As seen in Fig. 2, the proposed predictor is capable of performing very accurately even when the sampling period is relatively large. In comparison, the commonly used predictor method is less accurate, especially during transient operation, deteriorating the overall performance of the controller. In Fig. 2, it can also be observed that the circulating current in steady-state exhibits a worse behavior (low-frequency distortion) when bilinear terms are disregarded, which could affect the system losses. Specifically, an oscillation in the circulating current with approximately 10% magnitude can be observed when using a common predictor. Furthermore,

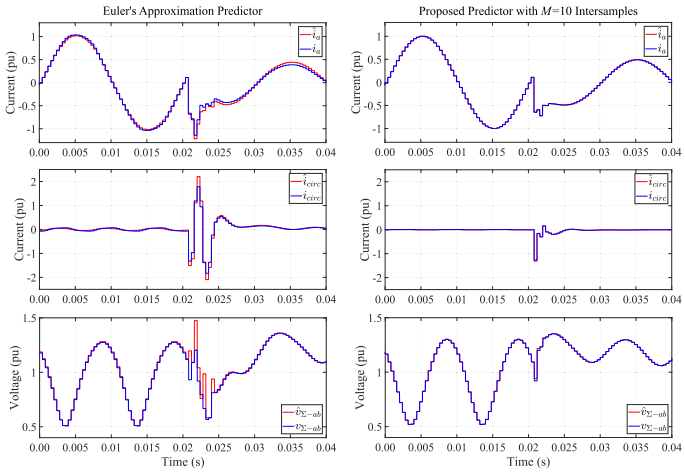

Fig. 2. Simulation waveforms for the proposed controller during a sudden reactive power change from full capacitive to half inductive operation at $t = 0.04$ s. Left plots: Predicted waveforms when using the common predictors (15) and (16). Right plots: Predicted waveforms when using the proposed predictors (19) and (20) with $M = 10$ intersamples. Top plots: Sampled injected current in phase a (blue) and its prediction (red). Middle plots: Sampled circulating current (blue) and its prediction (red). Bottom plot: Sampled cluster voltage in phase-arm ab (blue) and its prediction (red).

the harmonic content of the signals improves when bilinear terms are considered. Specifically, the total harmonic distortion (THD) of the StatCom currents improves from 1.46% to 0.30% at full capacitive power. One more observation from Fig. 2 is the large prediction errors in the capacitor voltages during transients when bilinear terms are not considered.

III. Constrained Model Predictive Control

This section presents a constrained control based on MPC for LC-StatComs that tracks the instantaneous real p and imaginary q power references, the instantaneous circulating current i_{circ} reference, and the cluster voltage $v_{\Sigma-x}$ references, while limiting the capacitor voltages and the arm currents during transients.

First, the control problem and the proposed hierarchical controller structure are described. Then, system objectives are mapped into cost functions and constraints, which, combined, define the optimization problem. Finally, using the proposed predictors (19) and (20), the optimization problem is formulated as a quadratic programming (QP) problem that can be solved using common methods such as interior-point methods, active-set methods, or ADMM. The interior-point methods have a per iteration cost generally much higher than the ADMM methods [26]. For this reason, an algorithm based on the ADMM has been chosen to do the experimental implementation.

A. Control Problem of the LC-StatCom

The LC-StatCom control is a challenging problem due to: 1) the large magnitude low-frequency voltage oscillation on the LC-StatCom capacitors, and 2) the nonnegligible coupling between the capacitor voltage dynamics and the inductor current dynamics. Thus, the proposed MPC deals with bilinear terms and has to satisfy the following control objectives:

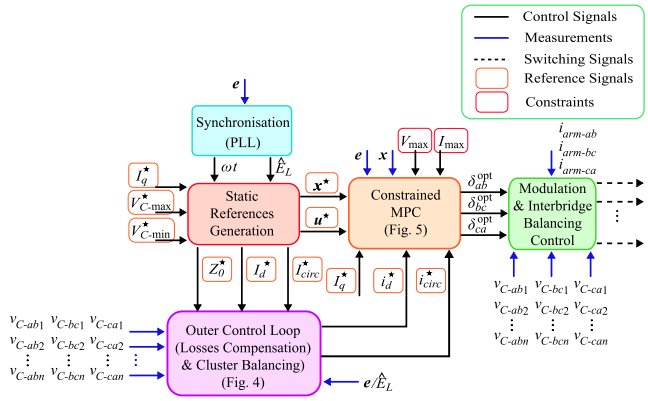

Fig. 3. Block diagram of the proposed constrained MPC using direct-power and outer loops.

1) regulation of the instantaneous powers/currents according to preestablished references;
2) high bandwidth control of the capacitor voltages;
3) capacitor voltage balancing (interphase and interbridge balancing);
4) maintaining the capacitor voltages and the arm currents within desired limits during transients.

The rest of this section discusses the proposed control to address this challenging problem in the LC-StatComs.

B. Controller Structure

Fig. 3 depicts the hierarchical control block diagram of the proposed constrained MPC applied to a multilevel LC-StatCom. Next, the main blocks are explained.

1) Constrained MPC: The main block of the control scheme is the "Constrained MPC" block. It computes in real time (in between samples) the optimal modulation functions for each converter phase-arm $\boldsymbol{u}^{\text{opt}} = [\,\delta_{ab}^{\text{opt}}\ \delta_{bc}^{\text{opt}}\ \delta_{ca}^{\text{opt}}\,]^T$ that minimize a quadratic cost function J subject to state and input constraints, and the discrete evolution of the bilinear state-space model (19). The optimization process is repeated every sampling period T_s according to the receding horizon policy. This leads to the following optimization problem:

$$\begin{aligned} \boldsymbol{u}^{\text{opt}}(k) = \arg\ &\underset{\boldsymbol{u}(k)}{\text{minimize}} \quad J \\ \text{subject to}\ &\hat{\boldsymbol{x}}\,(k+1) = \\ &\boldsymbol{A}_d\boldsymbol{x}(k) + \boldsymbol{B}_d\,(\boldsymbol{x}(k))\,\boldsymbol{u}(k) + \boldsymbol{W}_d\boldsymbol{e}(k) \\ &\hat{\boldsymbol{x}}\,(k+1) \in \mathbb{X} \\ &\boldsymbol{u}(k) \in \mathbb{U} \end{aligned} \tag{23}$$

where $\mathbb{X}$ and $\mathbb{U}$ represent the admissible domains, while $\hat{\boldsymbol{x}}(k+1)$ denotes the prediction of state $\boldsymbol{x}$ at instant $k+1$.

The optimal modulation functions δ_{ab}^{opt}, δ_{bc}^{opt}, δ_{ca}^{opt} constitute the inputs of block "Modulation & Interbridge Balancing Control," which generates the switching signals for the power converter.

The "Constrained MPC" block uses as input the actual state $\boldsymbol{x}(k)$ and voltage $\boldsymbol{e}(k)$, static references for the state $\boldsymbol{x}^{\star}(k)$ and the control $\boldsymbol{u}^{\star}(k)$, dynamic references for the active grid current component $i_d^{\star}$ and the circulating current $i_{\text{circ}}^{\star}$, and state

constraints for the capacitor voltages $V_{\max}$ and the arm currents $I_{\max}$. Static references assume steady-state operation and a set of nominal converter parameters, and they are calculated in block "Static References Generation," according to (7). Dynamic references aim to shape the static references in order to provide a set of correct references that properly regulate and balance the capacitor voltages despite converter parametric uncertainties. Dynamic references are calculated in the block "Outer Control Loop (Losses Compensation & Cluster Balancing)."

2) Static References Generation: The converter is synchronized with the PCC grid voltages by using a phase-locked loop to calculate the angle ωt and the amplitude $\hat{E}_L$. Subsequently, given the knowledge of the grid voltages, grid reactive power requirement $I_q^\star$, and the capacitor voltage maximum and minimum $V_{C-\max}^\star$ and $V_{C-\min}^\star$, coherent reference signals for the state variables and control inputs are calculated. The coherent reference signals agree with the aforementioned averaged model in (7); hence

$$\frac{d\boldsymbol{x}^\star}{dt} = \boldsymbol{A}\boldsymbol{x}^\star + \boldsymbol{B}\left(\boldsymbol{x}^\star\right)\boldsymbol{u}^\star + \boldsymbol{W}\boldsymbol{e} \tag{24}$$

where $\boldsymbol{x}^\star = [\, i_a^\star \; i_b^\star \; i_{\text{circ}}^\star \; v_{\Sigma-ab}^\star \; v_{\Sigma-bc}^\star \; v_{\Sigma-ca}^\star \,]^T$ represents the desired state trajectory, and $\boldsymbol{u}^\star$ is the applied controller action so that the system remains at the desired trajectory $\boldsymbol{x}^\star$.

The reference values according to (24) are calculated assuming that the grid voltages and the desired StatCom currents correspond to

$$\begin{bmatrix} e_{ab} \\ e_{bc} \\ e_{ca} \end{bmatrix} = \hat{E}_L \begin{bmatrix} \cos\left(\omega t + \pi/6\right) \\ \cos\left(\omega t - \pi/2\right) \\ \cos\left(\omega t + 5\pi/6\right) \end{bmatrix}$$
$$\begin{bmatrix} i_a^\star \\ i_b^\star \\ i_c^\star \end{bmatrix} = \hat{I}^\star \begin{bmatrix} \cos\left(\omega t + \varphi^\star\right) \\ \cos\left(\omega t + \varphi^\star - 2\pi/3\right) \\ \cos\left(\omega t + \varphi^\star + 2\pi/3\right) \end{bmatrix}. \tag{25}$$

Parameters $\hat{E}_L$ and $\hat{I}^\star$ represent the amplitudes of the line-to-line PCC grid voltages and the injected StatCom current references, respectively. The angle $\varphi^\star$ represents the phase difference between the injected currents and the line-to-neutral PCC voltages. Ideally, that is, without losses, $\varphi^\star$ is $\pi/2$ rad in inductive mode and $-\pi/2$ rad in capacitive mode, according to the direction of the currents indicated in Fig. 1.

The amplitude $\hat{I}^\star$ and angle $\varphi^\star$ of the desired injected StatCom currents in (25) can be calculated using their dq components. The q-component ($I_q^\star$) is a known grid requirement, and the d-component ($I_d^\star$) corresponds to

$$I_d^\star = -\frac{2\sqrt{2}\left(R_{\text{eq}} I_q^{\star 2} + P_0^\star\right)}{\hat{E}_L\left(1 + \sqrt{1 - 8R_{\text{eq}}\left(R_{\text{eq}} I_q^{\star 2} + P_0^\star\right)/\hat{E}_L^2}\right)} \tag{26}$$

where the power conservative $dq0$ transformation has been considered [11]. The power static reference $P_0^\star = 3R_{\text{arm}}(\hat{I}_{\text{circ}}^\star/\sqrt{2})^2$ corresponds to the increment of power in the converter when a static sinusoidal reference of circulating current $I_{\text{circ}}^\star$, with amplitude $\hat{I}_{\text{circ}}^\star$, is applied during steady-state [15].

Substituting (25) into (84), the arm current references $i_{\text{arm}-x}^\star$ can be calculated. Similarly, using (85), the converter voltage references $v_x^\star$ are derived. Once the arm current and converter voltage references are known, the cluster voltage references $v_{\Sigma-x}^\star$ can be calculated by solving the differential equation in (4), i.e.,

$$v_{\Sigma-x}^\star(t) = \sqrt{\left(v_{\Sigma-x}^\star(0)\right)^2 - \frac{2}{C/n}\int_0^t v_x^\star i_{\text{arm}-x}^\star dt} \tag{27}$$

for $x \in \{ab,\, bc,\, ca\}$, and where $v_{\Sigma-x}^\star(0)$ is the initial condition. Note that the integrator operator in (27) can be solved analytically, according to (25), (84), and (85). It is important to highlight that this reference design criterion stands in contrast with the commonly adopted approach in the conventional StatCom applications, where the capacitor voltages are regarded as constant due to the large capacitance used.

Using the following variable change:

$$z_{\Sigma-x}^\star = \frac{1}{2n}\left(v_{\Sigma-x}^\star\right)^2 \tag{28}$$

which is proportional to the capacitive energy stored in a converter phase, and solving (27) for (25) and $I_{\text{circ}}^\star = 0$, yields

$$\begin{bmatrix} z_{\Sigma-ab}^\star \\ z_{\Sigma-bc}^\star \\ z_{\Sigma-ca}^\star \end{bmatrix} = \begin{bmatrix} Z_0^\star \\ Z_0^\star \\ Z_0^\star \end{bmatrix} \mp \frac{S^\star}{6\omega_g C}\begin{bmatrix} \cos\left(2\left(\omega t + \pi/6 + \alpha_v^\star\right)\right) \\ \cos\left(2\left(\omega t - \pi/2 + \alpha_v^\star\right)\right) \\ \cos\left(2\left(\omega t + 5\pi/6 + \alpha_v^\star\right)\right) \end{bmatrix} \tag{29}$$

where the negative sign indicates the inductive mode while the positive sign is for the capacitive mode. Parameter $Z_0^\star$ is the mean square-capacitor voltage, i.e., $Z_0^\star = (z_{\Sigma-ab}^\star + z_{\Sigma-bc}^\star + z_{\Sigma-ca}^\star)/3$. Parameter $S^\star = (3/2)\hat{V}^\star(\hat{I}^\star/\sqrt{3})$ denotes the apparent power at the converter side, with $\hat{V}^\star$ and $\hat{I}^\star/\sqrt{3}$ as the amplitude of the fundamental-frequency converter voltage and arm current, respectively. Angle $\alpha_v^\star$ models the system losses and corresponds to the phase-shift between the line-to-line PCC voltages and the converter voltages.

As discussed in [2] and [11], it is convenient in the LC-StatComs to have a reference for $Z_0^\star$ that takes into account both normal and overload operating conditions. The reason is to ensure that the voltages across the capacitors have a preset maximum value at $V_{C-\max}^\star$ for any reactive power reference below the nominal value ($I_q^\star \le I_{q,n}$) and ensuring a preset minimum value at $V_{C-\min}^\star$ for overload conditions ($I_q^\star > I_{q,n}$). Consequently, according to (29), the reference for $Z_0^\star$ taking into account both operating conditions corresponds to [2]

$$Z_0^\star = \begin{cases} \frac{1}{2n}\left(nV_{C-\max}^\star\right)^2 - \frac{S^\star}{6\omega_g C}, & \text{if } I_q^\star \le I_{q,n} \\ \frac{1}{2n}\left(nV_{C-\min}^\star\right)^2 + \frac{S^\star}{6\omega_g C}, & \text{if } I_q^\star > I_{q,n}. \end{cases} \tag{30}$$

Once the cluster voltage references $v_{\Sigma-x}^\star$ and the converter voltage references $v_x^\star$ are known, the control reference $\delta_x^\star$ for each CHB is calculated as

$$\delta_x^\star = v_x^\star / v_{\Sigma-x}^\star. \tag{31}$$

3) Outer Control Loop—Dynamic References Generation: It is important to note that the above-mentioned static references consider a set of nominal parameters for capacitances, inductances, and resistances. Uncertainty in converter parameters can

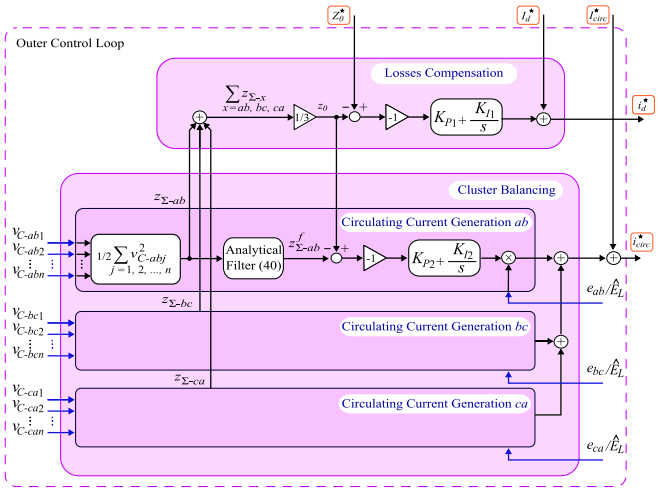

Fig. 4. Block diagram of the "Outer Control Loop" using the square sum capacitor voltages.

provide an incorrect reference to track by the MPC. Adding an outer loop represents a common approach in StatCom control that shapes the static references in order to provide a set of correct references [15]–[18]. Unlike the conventional StatCom outer loop control schemes, where the capacitor voltages are used as the variables to regulate, in the LC-StatComs, it is advisable to use the square-capacitor voltages [14], i.e.,

$$z_{C-xj} = \frac{1}{2} v_{C-xj}^2, \text{ and } z_{\Sigma-x} = \frac{1}{2} \sum_{j \in \mathcal{J}} v_{C-xj}^2. \tag{32}$$

Furthermore, the low capacitance values used in the LC-StatComs involve faster time constants in capacitor voltages. Therefore, the filtering of the capacitor voltage oscillations for control purposes must be faster in the LC-StatComs than in the conventional StatComs. Using conventional low-pass filtering schemes that can have a slow response could lead to transients where capacitor voltages are not properly regulated, which can, in turn, cause overmodulation or overvoltage issues. For this reason, the use of analytical feedforward filtering techniques [1], [8] represents a good alternative in the LC-StatComs.

Consequently, the outer control loop that provides a correct reference trajectory must change with respect to the conventional StatCom outer control loop. Specifically, Fig. 4 depicts the proposed "Outer Control Loop (Losses Compensation & Cluster Balancing)." Next, the importance of using the square-capacitor voltages is discussed.

The dynamics of the cluster voltages $v_{\Sigma-x}$, according to (4), can be written as the following power relationship:

$$p_x = -\frac{C}{n} v_{\Sigma-x} \frac{dv_{\Sigma-x}}{dt}, \text{ with } p_x = v_x i_{\text{arm}-x} \tag{33}$$

whose linearization around the equilibrium trajectory $V_{\Sigma-x}$ corresponds to

$$\tilde{p}_x \approx -\frac{C}{n} V_{\Sigma-x} \frac{d\tilde{v}_{\Sigma-x}}{dt} - \frac{C}{n} \tilde{v}_{\Sigma-x} \frac{dV_{\Sigma-x}}{dt} \tag{34}$$

where the bilinear terms have been considered negligible.

Obviously, in the conventional StatComs, the term $\frac{dV_{\Sigma-x}}{dt}$ is assumed to be zero, i.e., $V_{\Sigma-x}$ is assumed constant due to the large capacitances used, yielding a power-to-voltage relationship independent of the operating conditions. Therefore, since the term $\frac{dV_{\Sigma-x}}{dt}$ cannot be neglected in the LC-StatComs, considering the power-to-voltage transfer function as

$$\frac{\tilde{V}_{\Sigma-x}(s)}{\tilde{P}_x(s)} = -\frac{1}{C/n\, V_{\Sigma-x} s} \tag{35}$$

is not appropriate.

On the other hand, by using the square sum capacitor voltages (32), where the variable change $(C/n) v_{\Sigma-x} \dot{v}_{\Sigma-x} = C \dot{z}_{\Sigma-x}$ is used in (33), the dc-side relationship becomes linear and independent of the operating conditions, i.e.,

$$\frac{\tilde{Z}_{\Sigma-x}(s)}{\tilde{P}_x(s)} = -\frac{1}{sC} \tag{36}$$

which greatly simplifies the control design.

According to Fig. 4, $i_d^\star$ is calculated by regulating the mean square-capacitor voltage, that is, $z_0 = (z_{\Sigma-ab} + z_{\Sigma-bc} + z_{\Sigma-ca})/3$, to the static reference $Z_0^\star$ (30) so that the system losses are compensated. Namely, $i_d^\star$ is the output of a proportional-integral (PI) component plus static reference $I_d^\star$ (26), i.e.,

$$i_d^\star = \left(K_{P1} \tilde{z}_0 + K_{I1} \int \tilde{z}_0 dt \right) + I_d^\star \tag{37}$$

being the regulation error $\tilde{z}_0$

$$\tilde{z}_0 = z_0 - Z_0^\star \tag{38}$$

where $I_d^\star$, given in (26), has been added to the controller output to minimize control effort.

According to Fig. 4 and (36), choosing

$$K_{P1} = \frac{3C}{\hat{E}_L/\sqrt{2}} \frac{8}{T_{r1}}, \quad K_{I1} = \frac{3C}{\hat{E}_L/\sqrt{2}} \frac{16}{T_{r1}^2} \tag{39}$$

yields a critically damped closed-loop response with a settling time of approximately T_{r1}.

According to Fig. 4, $i_{\text{circ}}^\star$ is calculated by regulating the filtered component of each square sum capacitor voltages, namely $z_{\Sigma-ab}^f$, $z_{\Sigma-bc}^f$, $z_{\Sigma-ca}^f$, toward the mean square-capacitor voltage z_0 so that the energy of the capacitors is balanced between the converter phase arms. Particularly, the filtered square sum capacitor voltages are calculated as follows:

$$z_{\Sigma-x}^f = z_{\Sigma-x} - \Delta z_{\Sigma-x}^\star \tag{40}$$

with $\Delta z_{\Sigma-x}^\star$ referring to the twice fundamental harmonic component, i.e.,

$$\Delta z_{\Sigma-x}^\star = z_{\Sigma-x}^\star - Z_0^\star \tag{41}$$

with $z_{\Sigma-x}^\star$ according to (29).

According to [15], injecting a circulating current with a fundamental-frequency component generates active power capable of balancing the energy of the capacitors between phases. Specifically, $i_{\text{circ}}^\star$ to achieve cluster balance corresponds to

$$i_{\text{circ}}^\star = \sum_{x \in \mathcal{X}} \left(K_{P2} \tilde{z}_{\Sigma-x}^f + K_{I2} \int \tilde{z}_{\Sigma-x}^f dt \right) \frac{e_x}{\hat{E}_L} + I_{\text{circ}}^\star \tag{42}$$

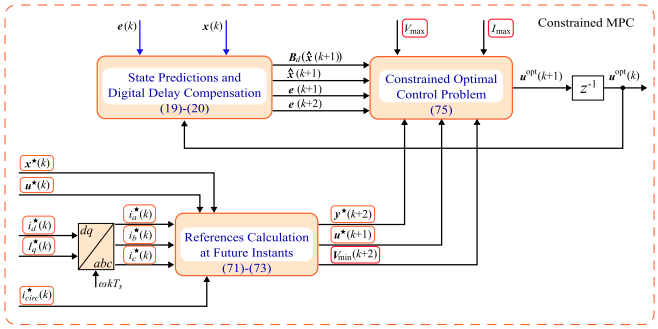

Fig. 5. Block diagram of the "Constrained MPC."

being $\tilde{z}^f_{\Sigma-x}$ the regulation error of the filtered square sum capacitor voltages, i.e.,

$$\tilde{z}^f_{\Sigma-x} = z^f_{\Sigma-x} - z_0. \tag{43}$$

Note that the normalized line-to-line PCC voltages e_{ab}, e_{bc}, e_{ca} modulate the PI outputs, i.e., $K_{P2}\tilde{z}^f_{\Sigma-x} + K_{I2}\int \tilde{z}^f_{\Sigma-x}dt$. Consequently, the product between each fundamental circulating current in (42) and the converter voltages v_{ab}, v_{bc}, v_{ca} leads to an active power distribution among the phases which steers each $z^f_{\Sigma-x}$ in the correct direction to balance the cluster voltages.

According to the experimental results, where the control action provided by the "Cluster Balancing" sub-block controller, when the cluster voltages are balanced, is zero, a proportional controller satisfies the control objective [27]. Therefore, according to Fig. 4 and (36), choosing

$$K_{P2} = \frac{2C}{\hat{E}_L}\frac{4}{T_{r2}}, \quad K_{I2} = 0 \tag{44}$$

yields a first-order closed-loop response with a settling time of approximately T_{r2}.

C. Predictor and Digital Delay Compensation

Fig. 5 depicts the structure of the "Constrained MPC" block. The optimization is performed over open-loop predictions, which are based on the accurate discrete-time model of the LC-StatCom discussed in the previous section, and defined in (19) and (20).

Obviously, in the prediction of $\boldsymbol{x}$ at instant $k+1$, i.e., $\hat{\boldsymbol{x}}(k+1)$, according to (19), the term $\boldsymbol{B}_d(\boldsymbol{x}(k))$ appears. According to (20) and due to the bilinear nature of the converter, the term $\boldsymbol{B}_d(\boldsymbol{x}(k))$ depends on the summation of state intersamples $\boldsymbol{x}(k+mT_s/M)$, which, in turn, depend on $\boldsymbol{u}(k)$. As $\boldsymbol{u}(k)$ is unknown at time instant k, $\boldsymbol{u}^{\text{opt}}(k-1)$ is assumed as its best estimation. This consideration is only valid for slow enough variations of the control signal $\boldsymbol{u}(k)$. This is related to the control bandwidth, which, in turn, is related to the penalization of the control signal within the cost function. Considering the true value of $\boldsymbol{u}(k)$ in the calculation of the intersample terms $\boldsymbol{x}(k+mT_s/M)$ would result in a nonlinear dependence on $\boldsymbol{u}(k)$, which would prevent the use of a QP approach in the optimization block, which will be explained in the next subsection.

Also, the proposed control takes into account the time delay required for A/D conversion plus control calculations when implementing a digital controller [28]. This means that once the state $\boldsymbol{x}$ and voltage $\boldsymbol{e}$ are measured at instant k, it is not possible to calculate $\boldsymbol{u}(k)$ instantly. In the sequel, this delay is considered to be of a sample time T_s. Nevertheless, the upcoming control $\boldsymbol{u}(k+1)$ can be calculated. This means that at instant k, the applied control input to the converter is well known as it was calculated in the previous sampling period, i.e., between $k-1$ and k. As a consequence, using the proposed predictor, the state $\boldsymbol{x}$ at $k+1$ can be predicted as $\hat{\boldsymbol{x}}(k+1)$. Similarly, the rotation matrix $\boldsymbol{R}_\omega$ can be used to exactly calculate the voltage $\boldsymbol{e}$ at $k+1$ as $\boldsymbol{e}(k+1) = \boldsymbol{R}^M_\omega \boldsymbol{e}(k)$. Hence, the state trajectory $\boldsymbol{x}$ at instant $k+2$ can be predicted as

$$\hat{\boldsymbol{x}}\,(k+2) = \boldsymbol{A}_d\hat{\boldsymbol{x}}\,(k+1) + \boldsymbol{B}_d\,(\hat{\boldsymbol{x}})\,\boldsymbol{u}\,(k+1) + \boldsymbol{W}_d\boldsymbol{e}\,(k+1) \tag{45}$$

with $\boldsymbol{B}_d(\hat{\boldsymbol{x}}) = \boldsymbol{B}_d(\hat{\boldsymbol{x}}(k+1))$ and matrices as in (20).

D. Cost Function and Constraints

The cost function constitutes one of the key elements in any MPC scheme since it establishes the desired behavior of the system during transient and steady-state operation.

The proposed cost function J consists of three terms, namely

$$J = J_1 + J_2 + J_3. \tag{46}$$

The first one, denoted as J_1, penalizes the predicted tracking error of the system output, that is, the difference between the output reference $\boldsymbol{y}^\star$ and the predicted output $\hat{\boldsymbol{y}}$. This term is given by

$$J_1 = \|\tilde{\boldsymbol{y}}\,(k+2)\|^2_{\boldsymbol{Q}_y} = \tilde{\boldsymbol{y}}\,(k+2)^T\,\boldsymbol{Q}_y\tilde{\boldsymbol{y}}\,(k+2) \tag{47}$$

where

$$\tilde{\boldsymbol{y}}(k) = \hat{\boldsymbol{y}}(k) - \boldsymbol{y}^\star(k). \tag{48}$$

The considered output vector corresponds to

$$\boldsymbol{y} = [p\ q\ i_{\text{circ}}\ v_{\Sigma-ab}\ v_{\Sigma-bc}\ v_{\Sigma-ca}]^T = \boldsymbol{C}\boldsymbol{x} \tag{49}$$

where the output matrix $\boldsymbol{C}$ corresponds to

$$\boldsymbol{C}(k) = \begin{bmatrix} \boldsymbol{C}_{11}(k) & \boldsymbol{0}_{2\times4} \\ \boldsymbol{0}_{4\times2} & \boldsymbol{I}_4 \end{bmatrix} \tag{50}$$

with submatrix $\boldsymbol{C}_{11}$ as

$$\boldsymbol{C}_{11} = \begin{bmatrix} e_a - e_c & e_b - e_c \\ \frac{1}{\sqrt{3}}\,(-e_a + 2e_b - e_c) & \frac{1}{\sqrt{3}}\,(-2e_a + e_b + e_c) \end{bmatrix}. \tag{51}$$

It can be noted that the terms of $\boldsymbol{C}$ depend linearly on the measured voltage $\boldsymbol{e}$. Note that the weighting matrix $\boldsymbol{Q}_y$ in (47) must be symmetric and positive semidefinite, i.e., $\boldsymbol{Q}_y \in \mathbb{S}_{\geq 0}$. Thus, the weighting matrix $\boldsymbol{Q}_y$ can be defined as

$$\boldsymbol{Q}_y = \text{diag}\,(\lambda_p,\ \lambda_q,\ \lambda_{i_{\text{circ}}},\ \lambda_{v_{\Sigma-ab}},\ \lambda_{v_{\Sigma-bc}},\ \lambda_{v_{\Sigma-ca}})\,. \tag{52}$$

As in [29] and [30], when directly controlling the instantaneous real and imaginary powers, the penalty on the corresponding two error tracking terms can be chosen equal, i.e., $\lambda_p = \lambda_q$.

Using the prediction model in (45), cost function (47) can be rewritten as a quadratic function in terms of the control input $\boldsymbol{u}(k+1)$.

It is also important to add a term in the cost function that penalizes the tentative control input $\boldsymbol{u}(k+1)$ with respect to its steady-state reference value $\boldsymbol{u}^{\star}(k+1)$, i.e., the control effort, which can provide a certain degree of robustness and stability [20], [31], [32].

Based on the previous reasoning, a second term in the cost function is added, which is denoted as J_2. This term is given by

$$J_2 = \|\tilde{\boldsymbol{u}}\,(k+1)\|^2_{\boldsymbol{R}} = \tilde{\boldsymbol{u}}\,(k+1)^T\,\boldsymbol{R}\tilde{\boldsymbol{u}}\,(k+1) \tag{53}$$

where

$$\tilde{\boldsymbol{u}}(k) = \boldsymbol{u}(k) - \boldsymbol{u}^{\star}(k). \tag{54}$$

Note that the weighting matrix $\boldsymbol{R}$ must be symmetric positive definite, i.e., $\boldsymbol{R} \in \mathbb{S}_{>0}$. Thus, the weighting matrix $\boldsymbol{R}$ can be defined as

$$\boldsymbol{R} = \lambda_u \boldsymbol{I}_3. \tag{55}$$

Note that cost function (53) is a quadratic function in terms of control input $\boldsymbol{u}(k+1)$.

One of the most attractive features of the MPC is its ability to deal with constraints in the optimal control determination.

One constraint is the modulation limits, i.e.,

$$-\boldsymbol{U}_3 \preceq \boldsymbol{u}\,(k+1) \preceq \boldsymbol{U}_3 \tag{56}$$

where $\boldsymbol{U}_3$ is a column vector of ones. This constraint defines a strict physical limitation of the converter.

Now, constraints on the arm currents and capacitor voltages are addressed. Upper and lower bounds at $I_{\max}$ and $I_{\min}$ are placed for the arm currents, while $V_{\max}$ and $V_{\min}$ define the upper and lower bounds for the cluster voltages. By aggregating the previous bounds in vectors, and using $I_{\min} = -I_{\max}$, yields

$$\begin{aligned} -I_{\max}\boldsymbol{U}_3 &\preceq \boldsymbol{C}_1\hat{\boldsymbol{x}}\,(k+2) \preceq I_{\max}\boldsymbol{U}_3 \\ \boldsymbol{V}_{\min}\,(k+2) &\preceq \boldsymbol{C}_2\hat{\boldsymbol{x}}\,(k+2) \preceq V_{\max}\boldsymbol{U}_3 \end{aligned} \tag{57}$$

with matrices corresponding to

$$\boldsymbol{C}_1 = \begin{bmatrix} 1/3 & -1/3 & 1 & 0 & 0 & 0 \\ 1/3 & 2/3 & 1 & 0 & 0 & 0 \\ -2/3 & -1/3 & 1 & 0 & 0 & 0 \end{bmatrix} \tag{58}$$

$$\boldsymbol{C}_2 = \begin{bmatrix} \boldsymbol{0}_3 & \boldsymbol{I}_3 \end{bmatrix} \tag{59}$$

and where the lower bound for the cluster voltages is time-varying

$$\boldsymbol{V}_{\min}(k) = \begin{bmatrix} |v^{\star}_{ab}(k)| \\ |v^{\star}_{bc}(k)| \\ |v^{\star}_{ca}(k)| \end{bmatrix}. \tag{60}$$

Note that references $\boldsymbol{y}^{\star} = \boldsymbol{C}\boldsymbol{x}^{\star}$ in (47) must be accordingly constrained to adhere to the operational limits, i.e.,

$$\begin{aligned} -I_{\max}\boldsymbol{U}_3 &\preceq \boldsymbol{C}_1\boldsymbol{x}^{\star}\,(k+2) \preceq I_{\max}\boldsymbol{U}_3 \\ \boldsymbol{V}_{\min}\,(k+2) &\preceq \boldsymbol{C}_2\boldsymbol{x}^{\star}\,(k+2) \preceq V_{\max}\boldsymbol{U}_3. \end{aligned} \tag{61}$$

It is important to note that the lower limit on the capacitor voltages in (57), and the modulation limits in (56), are different. If only (56) is imposed, the capacitor voltages are free to vary outside the envelopes (57) to a certain extent, and only the converter voltages should be chosen below the present cluster voltage values so as to minimize the objective cost function. The constraint in (57) creates a constraint on the envelope, meaning that no matter what power reference is desired to track, it should be impossible to drive the capacitor voltages out of the envelopes.

Using the prediction model in (45), the state constraints in (57) can be mapped into input constraints in the following way:

$$\boldsymbol{A}_c\boldsymbol{u}\,(k+1) \preceq \boldsymbol{b}_c \tag{62}$$

with constraints matrix $\boldsymbol{A}_c \in \mathbb{R}^{12\times 3}$ and constraints vector $\boldsymbol{b}_c \in \mathbb{R}^{12}$ corresponding to

$$\boldsymbol{A}_c = \begin{bmatrix} \boldsymbol{A}_{c1} \\ \boldsymbol{A}_{c2} \\ \boldsymbol{A}_{c3} \\ \boldsymbol{A}_{c4} \end{bmatrix} = \begin{bmatrix} \boldsymbol{C}_1\boldsymbol{B}_d\,(\hat{\boldsymbol{x}}) \\ -\boldsymbol{C}_1\boldsymbol{B}_d\,(\hat{\boldsymbol{x}}) \\ \boldsymbol{C}_2\boldsymbol{B}_d\,(\hat{\boldsymbol{x}}) \\ -\boldsymbol{C}_2\boldsymbol{B}_d\,(\hat{\boldsymbol{x}}) \end{bmatrix} \tag{63}$$

$$\boldsymbol{b}_c = \begin{bmatrix} \boldsymbol{b}_{c1} \\ \boldsymbol{b}_{c2} \\ \boldsymbol{b}_{c3} \\ \boldsymbol{b}_{c4} \end{bmatrix} = \begin{bmatrix} I_{\max}\boldsymbol{U}_3 - \boldsymbol{C}_1\boldsymbol{A}_d\hat{\boldsymbol{x}}\,(k+1) - \boldsymbol{C}_1\boldsymbol{W}_d\boldsymbol{e}\,(k+1) \\ I_{\max}\boldsymbol{U}_3 + \boldsymbol{C}_1\boldsymbol{A}_d\hat{\boldsymbol{x}}\,(k+1) + \boldsymbol{C}_1\boldsymbol{W}_d\boldsymbol{e}\,(k+1) \\ V_{\max}\boldsymbol{U}_3 - \boldsymbol{C}_2\boldsymbol{A}_d\hat{\boldsymbol{x}}\,(k+1) - \boldsymbol{C}_2\boldsymbol{W}_d\boldsymbol{e}\,(k+1) \\ -\boldsymbol{V}_{\min}\,(k+2) + \boldsymbol{C}_2\boldsymbol{A}_d\hat{\boldsymbol{x}}\,(k+1) + \boldsymbol{C}_2\boldsymbol{W}_d\boldsymbol{e}\,(k+1) \end{bmatrix} \tag{64}$$

with $\boldsymbol{B}_d(\hat{\boldsymbol{x}}) = \boldsymbol{B}_d(\hat{\boldsymbol{x}}(k+1))$. Note that the terms of $\boldsymbol{A}_c$ and $\boldsymbol{b}_c$ depend on the measured voltage $\boldsymbol{e}$ and measured state $\boldsymbol{x}$, and, hence, they need to be calculated online at each control period T_s.

To avoid nonfeasibility issues that can break the program in the controller implementation, the hard constraint in (62) is relaxed by adding a vector of surplus variables (or negative slack variable) in the optimization problem as

$$\begin{bmatrix} \boldsymbol{A}_{c1} \\ \boldsymbol{A}_{c2} \\ \boldsymbol{A}_{c3} \\ \boldsymbol{A}_{c4} \end{bmatrix} \boldsymbol{u} \preceq \begin{bmatrix} \boldsymbol{b}_{c1} \\ \boldsymbol{b}_{c2} \\ \boldsymbol{b}_{c3} \\ \boldsymbol{b}_{c4} \end{bmatrix} + \begin{bmatrix} \boldsymbol{\xi}_i \\ \boldsymbol{\xi}_i \\ \boldsymbol{\xi}_v \\ \boldsymbol{\xi}_v \end{bmatrix} \tag{65}$$

where the argument of $\boldsymbol{u}$, $\boldsymbol{\xi}_i$, and $\boldsymbol{\xi}_v$ is suppressed for brevity, being

$$\begin{aligned} \boldsymbol{\xi}_i &= \begin{bmatrix} \xi_i & \xi_i & \xi_i \end{bmatrix}^T \in \mathbb{R}^3_{\geq 0} \\ \boldsymbol{\xi}_v &= \begin{bmatrix} \xi_v & \xi_v & \xi_v \end{bmatrix}^T \in \mathbb{R}^3_{\geq 0} \end{aligned} \tag{66}$$

column vectors that group the nonnegative surplus terms for the corresponding states. Physically, the surplus terms $\boldsymbol{\xi}_i$, $\boldsymbol{\xi}_v$ represent how much the states exceed their bounds. Therefore, the surplus terms $\boldsymbol{\xi}_i, \boldsymbol{\xi}_v$ need to be strongly penalized within the cost function so that the soft constraints (65) keep the state variables almost as strictly within their bounds as hard constraints (62) do, while avoiding potential numerical and nonfeasibility issues.

Therefore, the new optimization variable is defined as

$$\boldsymbol{\mu}(k) = \begin{bmatrix} \boldsymbol{u}(k) \\ \boldsymbol{\xi}_i(k) \\ \boldsymbol{\xi}_v(k) \end{bmatrix} \in \mathbb{R}^9. \tag{67}$$

Consequently, the hard constraint (56), the soft constraint (65), and the nonnegativity condition for the surplus terms (66) can be grouped as the following equivalent set of linear inequality constraints on the optimization variable $\boldsymbol{\mu}$:

$$\begin{bmatrix} \boldsymbol{A}_{c1} & -\boldsymbol{I}_3 & \boldsymbol{0}_3 \\ \boldsymbol{A}_{c2} & -\boldsymbol{I}_3 & \boldsymbol{0}_3 \\ \boldsymbol{A}_{c3} & \boldsymbol{0}_3 & -\boldsymbol{I}_3 \\ \boldsymbol{A}_{c4} & \boldsymbol{0}_3 & -\boldsymbol{I}_3 \\ -\boldsymbol{I}_3 & \boldsymbol{0}_3 & \boldsymbol{0}_3 \\ \boldsymbol{I}_3 & \boldsymbol{0}_3 & \boldsymbol{0}_3 \\ \boldsymbol{0}_3 & -\boldsymbol{I}_3 & \boldsymbol{0}_3 \\ \boldsymbol{0}_3 & \boldsymbol{0}_3 & -\boldsymbol{I}_3 \end{bmatrix} \boldsymbol{\mu} \preceq \begin{bmatrix} \boldsymbol{b}_{c1} \\ \boldsymbol{b}_{c2} \\ \boldsymbol{b}_{c3} \\ \boldsymbol{b}_{c4} \\ \boldsymbol{U}_3 \\ \boldsymbol{U}_3 \\ \boldsymbol{0}_{3\times 1} \\ \boldsymbol{0}_{3\times 1} \end{bmatrix} \tag{68}$$

which ensures that: 1) the capacitor voltages and arm currents are maintained within desired envelopes (first four rows), 2) the modulation functions are within their physical limits (rows 5 and 6), and 3) the algorithm does not try to make $\boldsymbol{\xi}_i, \boldsymbol{\xi}_v$ negative (last two rows).

As the surplus variables are desired to be minimized, the following term needs to be added to the cost function:

$$J_3 = \|\boldsymbol{\xi}_i\|^2_{\boldsymbol{S}_i} + \|\boldsymbol{\xi}_v\|^2_{\boldsymbol{S}_v}. \tag{69}$$

Note that the weighting matrices $\boldsymbol{S}_i$ and $\boldsymbol{S}_v$ are symmetric positive definite, i.e., $\boldsymbol{S}_i \in \mathbb{S}_{>0}$ and $\boldsymbol{S}_v \in \mathbb{S}_{>0}$. Thus, the weighting matrices $\boldsymbol{S}_i$ and $\boldsymbol{S}_v$ can be defined as

$$\boldsymbol{S}_i = \lambda_{\xi_i} \boldsymbol{I}_3, \quad \boldsymbol{S}_v = \lambda_{\xi_v} \boldsymbol{I}_3. \tag{70}$$

To ensure that the soft constraints (65) are appropriately treated, the penalties λ_{ξ_i} and λ_{ξ_v} are chosen large enough.

E. Calculation of Future Reference Values

Cost function $J_1 + J_2$ [(47) and (53)] depends on future values of the state reference and control input reference. Moreover, the lower limit (60) for the capacitor voltage constraints (57) also depend on future values of the references. Obviously, the values of the state reference $\boldsymbol{x}^\star$ and the control reference $\boldsymbol{u}^\star$ at future instants are unknown at the instant of measurement k, and a calculation is needed.

The concept of the rotation matrix $\boldsymbol{R}_\omega$ (21) can be used here to calculate future values of the reference signals. For example, the injected StatCom current references at instant $k+1$ can be calculated as follows:

$$\begin{bmatrix} i_a^\star(k+1) \\ i_b^\star(k+1) \\ i_c^\star(k+1) \end{bmatrix} = \boldsymbol{R}_\omega^M \begin{bmatrix} i_a^\star(k) \\ i_b^\star(k) \\ i_c^\star(k) \end{bmatrix}. \tag{71}$$

Similarly, the converter voltage references (85) at future instants can be calculated as follows:

$$\begin{bmatrix} v_{ab}^\star(k+1) \\ v_{bc}^\star(k+1) \\ v_{ca}^\star(k+1) \end{bmatrix} = \boldsymbol{R}_\omega^M \begin{bmatrix} v_{ab}^\star(k) \\ v_{bc}^\star(k) \\ v_{ca}^\star(k) \end{bmatrix}. \tag{72}$$

Regarding the future values for the cluster voltage references, it is easier to calculate them indirectly through the square sum capacitor voltage references (29). The mean square-capacitor voltage $Z_0^\star$ is constant in time (30), whereas the twice fundamental harmonic $\Delta z_{\Sigma-x}^\star$ (41) at instant $k+1$ can be calculated as

$$\begin{bmatrix} \Delta z_{\Sigma-ab}^\star(k+1) \\ \Delta z_{\Sigma-bc}^\star(k+1) \\ \Delta z_{\Sigma-ca}^\star(k+1) \end{bmatrix} = \boldsymbol{R}_{-2\omega}^M \begin{bmatrix} \Delta z_{\Sigma-ab}^\star(k) \\ \Delta z_{\Sigma-bc}^\star(k) \\ \Delta z_{\Sigma-ca}^\star(k) \end{bmatrix} \tag{73}$$

with $\boldsymbol{R}_{-2\omega}$ being a rotation matrix that considers the double frequency and negative sequence of the square sum capacitor voltages, i.e.,

$$\boldsymbol{R}_{-2\omega} = \boldsymbol{T}_{\alpha\beta}^\dagger \begin{bmatrix} \cos\left(-2\omega\frac{T_s}{M}\right) & -\sin\left(-2\omega\frac{T_s}{M}\right) \\ \sin\left(-2\omega\frac{T_s}{M}\right) & \cos\left(-2\omega\frac{T_s}{M}\right) \end{bmatrix} \boldsymbol{T}_{\alpha\beta}. \tag{74}$$

Consequently, the cluster voltage references at future instants can be calculated using (28). Subsequently, $\boldsymbol{u}^\star$ at future instants is calculated using (31).

F. Constrained Optimization Problem

Combining the cost function in (47), (53), and (69), the constraints in (68), and the new optimization variable $\boldsymbol{\mu}$ in (67), the initial optimization problem depicted in (23) becomes

$$\begin{aligned} &\boldsymbol{\mu}^{\text{opt}}(k+1) = \arg\underset{\boldsymbol{\mu}}{\text{minimize}} \quad (1/2)\,\boldsymbol{\mu}^T \boldsymbol{H} \boldsymbol{\mu} + \boldsymbol{f}^T \boldsymbol{\mu} \\ &\text{subject to } (68) \end{aligned} \tag{75}$$

where the argument of $\boldsymbol{\mu}$ is suppressed for brevity, and the Hessian matrix $\boldsymbol{H}$ and the gradient vector $\boldsymbol{f}$ correspond to

$$\boldsymbol{H} = \begin{bmatrix} \boldsymbol{H}_{11} & \boldsymbol{0}_3 & \boldsymbol{0}_3 \\ \boldsymbol{0}_3 & \boldsymbol{S}_i & \boldsymbol{0}_3 \\ \boldsymbol{0}_3 & \boldsymbol{0}_3 & \boldsymbol{S}_v \end{bmatrix}, \quad \boldsymbol{f} = \begin{bmatrix} \boldsymbol{f}_1 \\ \boldsymbol{0}_{3\times 1} \\ \boldsymbol{0}_{3\times 1} \end{bmatrix} \tag{76}$$

where the Hessian submatrix $\boldsymbol{H}_{11}$ and gradient vector $\boldsymbol{f}_1$ correspond to

$$\begin{aligned} &\boldsymbol{H}_{11} = \boldsymbol{B}_d(\hat{\boldsymbol{x}})^T \boldsymbol{Q}_x \boldsymbol{B}_d(\hat{\boldsymbol{x}}) + \lambda_u \boldsymbol{I}_3 \\ &\boldsymbol{f}_1 = \boldsymbol{B}_d(\hat{\boldsymbol{x}})^T \boldsymbol{Q}_x \\ &(\boldsymbol{A}_d \hat{\boldsymbol{x}}(k+1) - \boldsymbol{x}^\star(k+2) + \boldsymbol{W}_d \boldsymbol{e}(k+1)) \\ &-\lambda_u \boldsymbol{u}^\star(k+1) \end{aligned} \tag{77}$$

with $\boldsymbol{B}_d(\hat{\boldsymbol{x}}) = \boldsymbol{B}_d(\hat{\boldsymbol{x}}(k+1))$, and $\boldsymbol{Q}_x = \boldsymbol{Q}_x(k+2)$, where

$$\boldsymbol{Q}_x(k) = \boldsymbol{C}(k)^T \boldsymbol{Q}_y \boldsymbol{C}(k). \tag{78}$$

Note that the terms of $\boldsymbol{H}$ and $\boldsymbol{f}$ depend on the measured voltage $\boldsymbol{e}$ and measured state $\boldsymbol{x}$, and, hence, they need to be calculated online at each control period T_s.

As the function to minimize is quadratic and the optimization is subject to linear inequality constraints, the resulting optimization problem (75) constitutes a QP problem.

The result of the optimization is the sequence of optimal control inputs $\boldsymbol{u}$ and surplus terms $\boldsymbol{\xi}_i$, $\boldsymbol{\xi}_v$, according to (67). The first three elements of the optimization variable correspond to $\boldsymbol{u}^{\text{opt}} = [\,\delta_{ab}^{\text{opt}}\ \delta_{bc}^{\text{opt}}\ \delta_{ca}^{\text{opt}}\,]^T$, which are implemented at instant k and sent to the "Modulation & Interbridge Balancing Control" block.

TABLE I
EXPERIMENTAL SYSTEM PARAMETERS

Parameter	Value
Nominal line-to-line PCC voltage amplitude, $\hat{E}_{L,n}$	$30\sqrt{2}\sqrt{3}$ V (1 p.u.)
Grid nominal power, $S_{g,n}$	636 VA (1 p.u.)
Grid angular frequency, ω_g	20π rad/s
Number of submodules per phase, n	1
Individual switch switching frequency, f_{sw}	20 kHz
Controller sampling period, T_s	500 μs
Maximum capacitor voltage reference, $V^{\star}_{C-\max}$	$1.3\hat{E}_{L,n}/n = 95.5$ V
Capacitance per H-bridge, C	0.96 mF ($r_n = 0.6$)
Filter inductances, L / L_{arm}	5 mH (0.075 p.u.) / 5 mH (0.075 p.u.)
Parasitic resistances, R / R_{arm}	150 mΩ (0.035 p.u.) / 150 mΩ (0.035 p.u.)

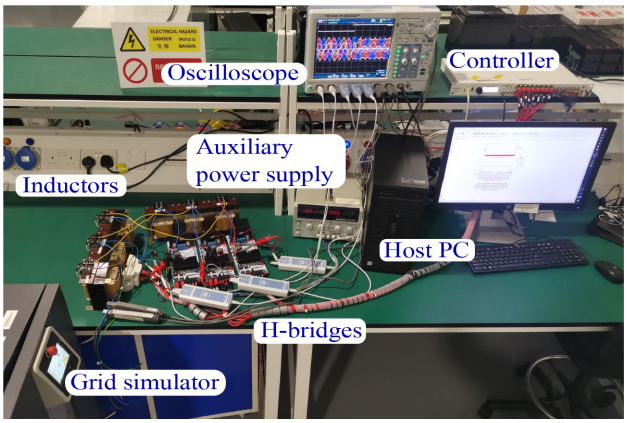

Fig. 6. Experimental system setup.

IV. EXPERIMENTAL RESULTS

With the purpose of assessing the proposed constrained MPC approach to control three-phase LC-StatComs, both in steady-state and during transients, this section describes the measurements that illustrate the controller behavior concerning its ability to provide fast transient responses while fulfilling the design constraints.

A. System and Control Parameters

The LC-StatCom laboratory prototype is connected to a 30-V grid, and it has a rated apparent power of approximately 700 VA. Table I summarizes the system parameters and Fig. 6 shows the experimental setup. The inductors have been sized to provide a rated voltage drop of approximately 10% between the converter ac-side voltage and the PCC grid voltage.

The PCC grid voltage is provided by a GE&EL 15 kVA CINERGIA grid emulator. In this setup, three IMPERIX PEH2015 H-bridge converters were used to construct a three-level LC-StatCom with delta configuration, with the dc-link capacitor of $C = 0.96$ mF. The capacitors operate at a peak voltage reference of $V^{\star}_{C-\max} = 95.5$ V. The value of the dc-link capacitance C has been designed for a nominal low-frequency voltage ripple of 60%, i.e., $r_n = 0.6$ [33], according to

$$C = \frac{2S_n}{3n}\frac{1}{\omega_g V^{\star 2}_{C-\max} r_n\,(2 - r_n)} \tag{79}$$

with S_n as the rated converter power (corresponding to approximately 700 VA in the experimental setup).

The control functions were implemented in a B-Box RCP 3.0 board from IMPERIX. The B-Box RCP has a dual-core DSP (2× ARM Cortex A9 1 GHz, 1 GB DDR3), in which the MPC controller is implemented with 2-kHz sampling. This means that the pulsewidth modulation (PWM) inputs, i.e., the voltages corresponding to the duty cycles, are generated at a sample rate of 2 kHz. The PWM is implemented in a Kintex-grade FPGA (Xilinx Kintex 7 125 K) with a time resolution of 4 ns, using a 20-kHz 32-b triangular carrier. To solve the optimization problem, an open-source convex QP solver, OSQP [34], [35], based on ADMM, was programmated. Predictions are calculated using the proposed predictor with $M = 6$ intersamples, and the maximum number of iterations of the OSQP solver has been set to 20, which represents approximately 90% of the available computational resources when using a sample rate of 2 kHz.

The weighting factors used in the predictive controller to trade off the different control objectives [according to (52) for the output error penalization, to (55) for the control effort penalization, and to (70) for the surplus variables] have the following values:

$$\begin{aligned} &\lambda_p = \lambda_q = 20/S^2_{g,n}, \quad \lambda_{i_{\text{circ}}} = 3/\left(\hat{I}_n/\sqrt{3}\right)^2 \\ &\lambda_{v_{\Sigma-ab}} = \lambda_{v_{\Sigma-bc}} = \lambda_{v_{\Sigma-ca}} = 0 \\ &\lambda_u = 1, \quad \lambda_{\xi_i} = \lambda_{\xi_v} = 10^6 \end{aligned} \tag{80}$$

with $S_{g,n} = 636$ VA and $\hat{I}_n = 10$ A according to Table I.

Regarding the block "Outer Control Loop (Losses Compensation & Cluster Balancing)" that provides dynamic references to the predictive control (as depicted in Fig. 4), the control parameters in (39) and (44) have been used for a response time of $T_{r1} = 2.5(2\pi/\omega_g)$ s in the "Losses Compensation" sub-block and $T_{r2} = 1.5(2\pi/\omega_g)$ s in the "Cluster Balancing" sub-block. These parameter values show an excellent tradeoff between

TABLE II
CAPACITANCE UNCERTAINTY ERROR. CASE I: 10% UNCERTAINTY IN THE CAPACITANCE PARAMETER IN ONE SUBMODULE IN PHASE *ab* ; CASE II: 10% UNCERTAINTY IN THE CAPACITANCE PARAMETER IN THREE SUBMODULES IN PHASE *ab* ; CASE III: 10% UNCERTAINTY IN THE CAPACITANCE PARAMETER IN EACH SUBMODULE IN PHASE *ab*

	Instantaneous Maximum Error (%)			Mean Deviation (%)		
Case	*ab*	*bc*	*ca*	*ab*	*bc*	*ca*
I	4.1	2.0	2.4	1.3	0.8	0.8
II	11.2	3.9	7.6	3.2	1.5	2.7
III	17.8	6.0	13.2	5.3	2.2	4.8

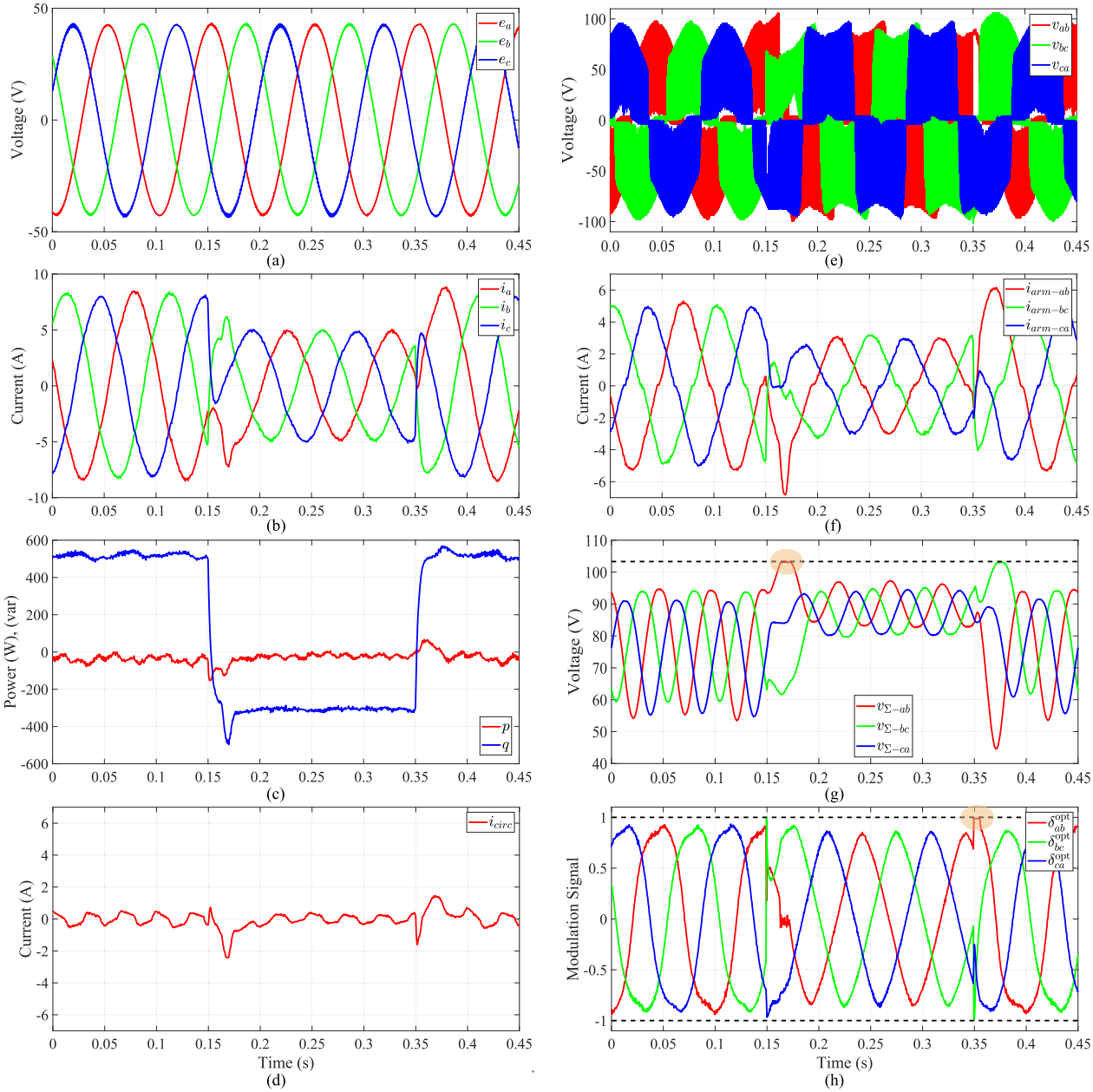

Fig. 7. Experimental waveforms during a sudden reactive power change from 80%-rated power capacitive mode to 40%-rated power inductive mode at $t = 0.15$ s and vice versa at $t = 0.35$ s. (a) Line-to-neutral PCC voltages e_a, e_b, e_c. (b) Injected StatCom currents i_a, i_b, i_c. (c) Instantaneous powers p, q. (d) Circulating current i_{circ}. (e) PWM converter voltages v_{ab}, v_{bc}, v_{ca}. (f) Arm currents $i_{\text{arm}-ab}$, $i_{\text{arm}-bc}$, $i_{\text{arm}-ca}$. (g) Capacitor voltages $v_{\Sigma-ab}$, $v_{\Sigma-bc}$, $v_{\Sigma-ca}$. (h) Optimal modulation signals δ_{ab}^{opt}, δ_{bc}^{opt}, δ_{ca}^{opt}.

overshoot and speed response of the expected active grid current component $i_d^\star$ and circulating current $i_{\text{circ}}^\star$.

B. Dynamic Performance

The operation of the proposed constrained predictive controller is tested under an abrupt change in the instantaneous imaginary power reference $q^\star$, from 80%-rated power capacitive-mode to 40%-rated power inductive mode, and then a return to 80%-rated power capacitive mode. Fig. 7 shows the experimental waveforms. The top capacitor voltage bound $V_{\max}$ is fixed at 40% over the nominal line-to-line PCC voltage, i.e., $V_{\max} = 1.4\hat{E}_{L,n}$, which corresponds to the state constraint in (57). This bound, which is indicated in Fig. 7(g) with a dashed line, is of paramount interest in the LC-StatComs because it allows one to reduce the capacitor size and simultaneously operate in a safe range that prevents overvoltages on capacitors and semiconductors. Current waveforms also remain within their prescribed bounds. The magnitude of the current bound is chosen to be $I_{\max} = 1.5\hat{I}_n/\sqrt{3}$, which corresponds to the state constraint in (57). The current bound has been chosen to protect the power semiconductor, thus limiting the peak arm current.

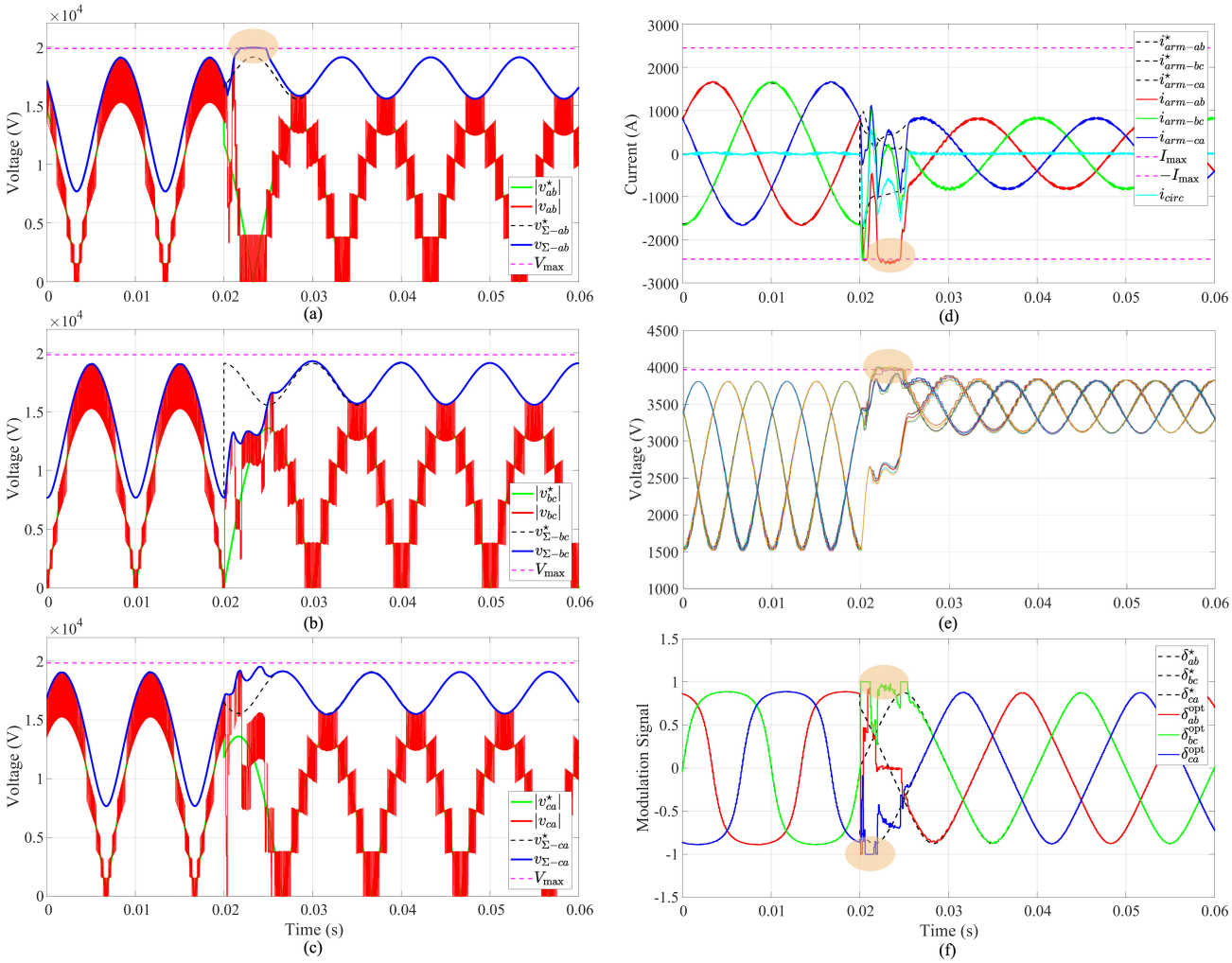

Fig. 8. LC-StatCom simulation waveforms, when using the proposed constrained MPC, during a sudden reactive power change from 100%-rated power capacitive mode to 50%-rated power inductive mode at $t = 0.02$ s. (a) Phase-arm ab voltages v_{ab}, $v_{\Sigma-ab}$. (b) Phase-arm bc voltages v_{bc}, $v_{\Sigma-bc}$. (c) Phase-arm ca voltages v_{ca}, $v_{\Sigma-ca}$. (d) Arm currents $i_{\text{arm}-ab}$, $i_{\text{arm}-bc}$, $i_{\text{arm}-ca}$. (e) Fifteen individual capacitor voltages. (f) Optimal modulation signals δ_{ab}^{opt}, δ_{bc}^{opt}, δ_{ca}^{opt}.

It can be observed that the fundamental-frequency components of the converter voltages v_{ab}, v_{bc}, v_{ca} [Fig. 7(e)] are in phase with their respective capacitor voltages $v_{\Sigma-ab}$, $v_{\Sigma-bc}$, $v_{\Sigma-ca}$ [Fig. 7(g)] when operating in the capacitive region, whilst the converter voltages are in counterphase with the capacitor voltages during inductive mode. It can be observed that the changes that occur in $t = 0.15$ s and $t = 0.35$ s are almost instantaneous. Also, it can be appreciated that due to the low capacitance used, the capacitor voltages present an oscillation above 50% of their dc values during capacitive operation.

It is worth noting that the transient response of the injected currents i_a, i_b, i_c and instantaneous powers p, q at $t = 0.15$ s, as shown in Fig. 7(b) and (c), is very fast, with a settling time for the reactive power of less than one-fifth of the fundamental period. It happens, despite the fact that the cluster voltage $v_{\Sigma-ab}$ is bounded by its top limit $V_{\max}$ at $t = 0.163$ s for one-tenth of the fundamental period approximately, as illustrated in Fig. 7(g). It can be seen that the modulation signal δ_{ab}^{opt} is close to zero while $v_{\Sigma-ab} = V_{\max}$ is bounded, as shown in Fig. 7(h), which is in agreement with the capacitor voltage dynamics in (4). Also, note that when the cluster voltage $v_{\Sigma-ab}$ is bounded, the injected currents and instantaneous power, as shown in Fig. 7(b) and (c), deviate from their expected references. This result highlights the tradeoff inherent with the proposed approach, i.e., the ability to constrain state variables causes some temporary tracking error in the output power and currents.

The transient response of the injected currents i_a, i_b, i_c and instantaneous powers p, q at $t = 0.35$ s, as shown in Fig. 7(b) and (c), is also very fast, with a settling time for the reactive power of less than one-tenth of the fundamental period. However, in this transient, state constraints (57) are not active. On the contrary, the constraint that limits the modulation signal δ_{ab}^{opt} in the range $[-1,\ 1]$ is active at $t = 0.35$ s for approximately one-twentieth of the fundamental period, according to (56). This result demonstrates the MPC ability to constrain the inputs. Also, note that the modulation signal range can be modified by changing its bounds, according to (56).

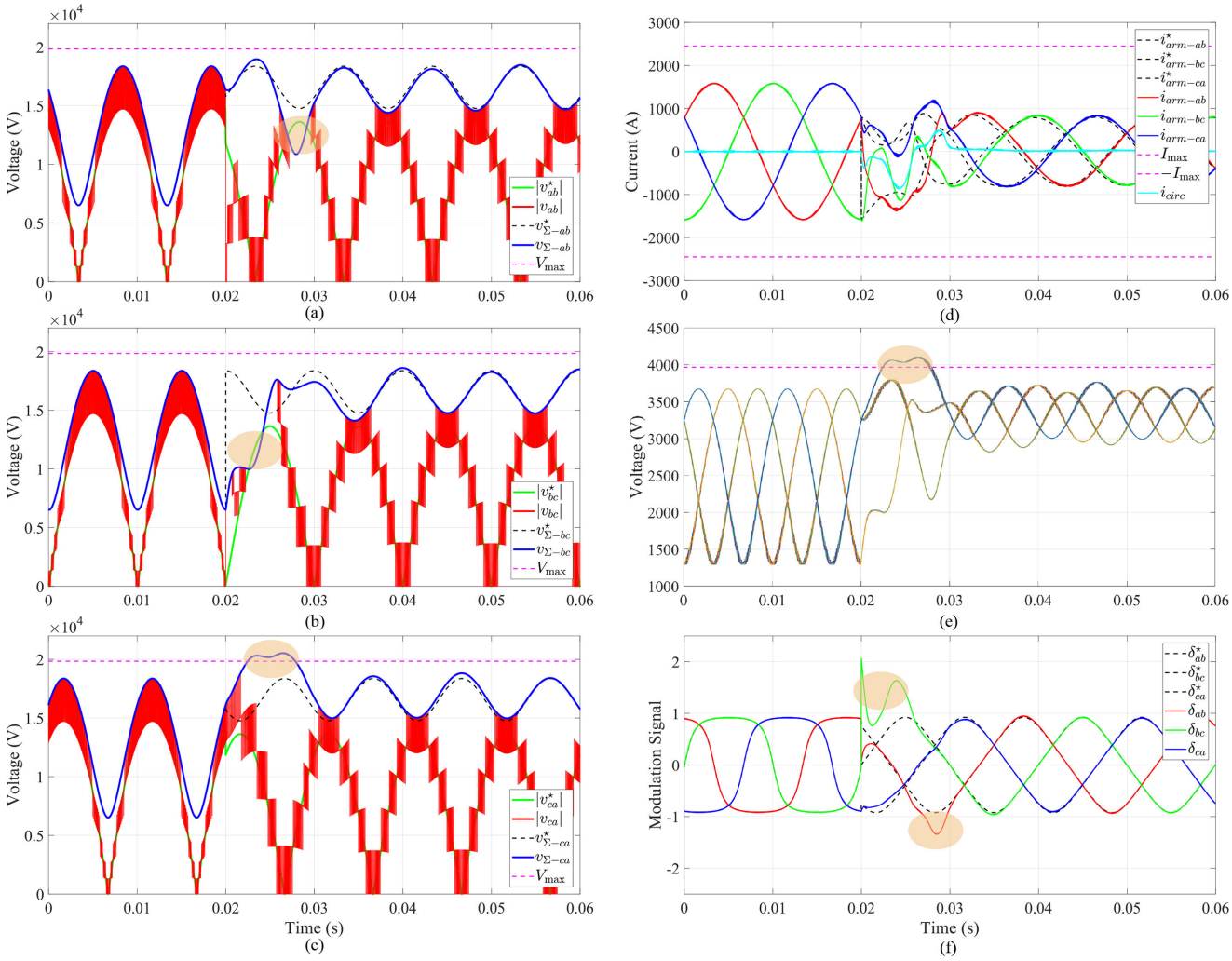

Fig. 9. LC-StatCom simulation waveforms, when using a current control designed in the synchronous *dq* frame with the conventional decoupled control, during a sudden reactive power change from 100%-rated power capacitive mode to 50%-rated power inductive mode at $t = 0.02$ s. (a) Phase-arm ab voltages v_{ab}, $v_{\Sigma-ab}$. (b) Phase-arm bc voltages v_{bc}, $v_{\Sigma-bc}$. (c) Phase-arm ca voltages v_{ca}, $v_{\Sigma-ca}$. (d) Arm currents $i_{\text{arm}-ab}$, $i_{\text{arm}-bc}$, $i_{\text{arm}-ca}$. (e) Fifteen individual capacitor voltages. (f) Modulation signals δ_{ab}, δ_{bc}, δ_{ca}.

Therefore, the experimental measures show fast transients and the capability of limiting the state variables and the inputs, which is of paramount importance in the LC-StatComs.

V. Complimentary Simulations

In this section, additional simulation results for a 36-MVA multilevel LC-StatCom with five submodules per phase are provided to demonstrate the effectiveness of the proposed constrained MPC to limit the individual capacitor voltages during transient operation when multiple submodules are used. The parameters of the simulated system are the same (in per-unit system) to those used in the experiment (given in Table I) but for a 6-kV 50-Hz grid. The system is simulated in the MATLAB/Simulink environment using a sampling rate of 10 kHz. Predictions are calculated using the proposed predictor with $M = 10$ intersamples.

The block "Modulation & Interbridge Balancing Control" in Fig. 3 is implemented using a phase-shifted carrier PWM strategy as in [14] with 1 -kHz carriers.

The waveforms for the case when $q^\star$ changes from 100%-rated power capacitive mode to 50%-rated power inductive mode at $t = 0.02$ s are shown in Fig. 8.

Similar to the experimental results, the cluster voltage $v_{\Sigma-ab}$ is bounded by its top limit $V_{\max}$ at $t = 0.021$ s for one-fifth of the fundamental period approximately, as illustrated in Fig. 8(a). Consequently, the five individual capacitor voltages embedded in phase-arm ab are also bounded by their top limit $V_{\max}/n$, as illustrated in Fig. 8(e). It can be seen that the optimal modulation signal δ_{ab}^{opt} calculated by the MPC is close to zero while $v_{\Sigma-ab} = V_{\max}$, as shown in Fig. 8(f). While the capacitor voltages are temporarily bounded, the currents do not follow the expected reference, as shown in Fig. 8(d), reaching the extreme case where the arm current $i_{\text{arm}-ab}$ is bounded by its bottom limit $I_{\min}$ at $t = 0.021$ s for one-fifth of the fundamental period approximately.

The above simulation results are in agreement with the experimental results shown in Fig. 7, thus corroborating that the proposed method can correctly work when multiple submodules are used.

For the sake of completeness, the LC-StatCom performance when using the proposed constrained MPC is compared to that obtained when using a more traditional control based on linear control. Specifically, the structure of the controller is exactly the same as that of the proposed MPC, which corresponds to Fig. 3, but the "Constrained MPC" block is replaced by a current control loop designed in the synchronous dq frame with the conventional decoupled control. The PI gains for the dq current controllers were designed for a 2 -ms response time.

The linear controller is able to regulate the LC-StatCom and balance its capacitor voltages, despite the multiple saturations that take place during the transient. For example, the cluster voltage $v_{\Sigma-ab}$ becomes lower than its ac-side reference $|v^{\star}_{ab}|$ at $t = 0.027$ s for one-tenth of the fundamental period approximately, as illustrated in Fig. 9(a). It can be seen that the corresponding modulation signal δ_{ab} is outside the range $[-1,\ 1]$ while $v_{\Sigma-ab} < |v^{\star}_{ab}|$, as shown in Fig. 9(f). The same phenomenon occurs in phase-arm bc, as can be seen in Fig. 9(b) and (f). Unlike the proposed constrained MPC, the conventional linear control lacks the ability to limit state variables, as it can be observed how the cluster voltage $v_{\Sigma-ca}$ exceeds its top limit, and accordingly so the five individual capacitor voltages embedded in phase-arm ca do, as illustrated in Fig. 9(c) and (e). As it can be seen in Fig. 9, the arm currents take approximately a complete cycle to settle to their reference values, while the proposed control offers transient responses of less than a quarter of the fundamental period. This delay of a period is caused by distorted capacitor voltages during this time.

For the sake of completeness, three different cases with 10% uncertainty in the capacitance parameter have been studied in simulation and the results, at full capacitive mode, which are summarized in Table II. *Case I* where only one capacitor in phase-arm *ab* deviates 10% from its nominal value; *Case II* where three capacitors in phase-arm *ab* deviate 10%; *Case III* where all the capacitors in phase-arm *ab* deviate 10%. The worst-case scenario, which corresponds to *Case III*, presents a maximum error in instantaneous capacitor voltages lower than 18.0%, 6.0%, and 13.5%, in phase-arms *ab*, *bc*, and *ca*, respectively, with respect to their nominal references, and a mean deviation lower than 5.5%, 2.5%, and 5.0% within a fundamental period. None of the cases showed any significative error in the current waveforms. In addition, despite the parametric uncertainty, waveforms showed fast and stable transients, and that capacitor voltages were properly limited by the proposed constrained MPC.

VI. Conclusion

A constrained MPC approach for the control of three-phase multilevel LC-StatComs has been implemented, specifically for CHB converters with delta configuration. The proposed MPC approach considers the bilinear nature of the LC-StatComs. The article shows how the accuracy of the model predictions improves by applying the proposed concept of intersampling. Furthermore, the proposed MPC approach considers the reference design and the adaptation of the outer control loop to LC-StatComs. Moreover, a comprehensive set of control design constraints adapted to the LC-StatCom has been proposed. The constrained MPC approach results in fast transient response and the ability to constrain the voltage value across the relatively small capacitors. The article has presented a comprehensive set of experimental measures that corroborates computational feasibility. For the reported cases, the proposed predictions enhancement results in the elimination of steady-state oscillations in the circulating current of approximately 10% and improvement in the THD of the grid currents from 1.46% to 0.30% (80% improvement). Also, simulation results show the improved performance of the proposed MPC compared with a more conventional control approach based on PI regulators in the *dq* frame. For the studied cases, the proposed approach is approximately four times faster in current transients, while it is able to limit the individual capacitor voltages. Therefore, the proposed MPC can be an effective solution to control LC-StatComs, providing good dynamic performance while effectively containing the capacitor voltages and arm currents within safe operating regions, as experimental and simulation results have corroborated.

Appendix
Dynamic Current Equations

This appendix provides the differential equations of the three independent currents of the bilinear CHB system model with continuous variables in (7), i.e., $i_a,\ i_b,\ i_{\text{circ}}$.

From the circuit shown in Fig. 1, the instantaneous three-phase PWM converter voltages $v_{ab},\ v_{bc},\ v_{ca}$ can be obtained as

$$\begin{bmatrix} v_{ab} \\ v_{bc} \\ v_{ca} \end{bmatrix} = L_{\text{arm}} \frac{d}{dt} \begin{bmatrix} i_{\text{arm}-ab} \\ i_{\text{arm}-bc} \\ i_{\text{arm}-ca} \end{bmatrix} + R_{\text{arm}} \begin{bmatrix} i_{\text{arm}-ab} \\ i_{\text{arm}-bc} \\ i_{\text{arm}-ca} \end{bmatrix} + \boldsymbol{E}_1 \left(L \frac{d}{dt} \begin{bmatrix} i_a \\ i_b \\ i_c \end{bmatrix} + R \begin{bmatrix} i_a \\ i_b \\ i_c \end{bmatrix} + \begin{bmatrix} e_a \\ e_b \\ e_c \end{bmatrix} \right) \tag{81}$$

with

$$\boldsymbol{E}_1 = \begin{bmatrix} 1 & -1 & 0 \\ 0 & 1 & -1 \\ -1 & 0 & 1 \end{bmatrix}. \tag{82}$$

The injected StatCom currents $i_a,\ i_b,\ i_c$ are linear combinations of the arm currents $i_{\text{arm}-ab},\ i_{\text{arm}-bc},\ i_{\text{arm}-ca}$; the phase a injected current, for example, is given by $i_a = i_{\text{arm}-ab} - i_{\text{arm}-ca}$. The injected currents for the phases b and c are defined accordingly. Further analyzing the relationship between the arm currents and the injected StatCom currents and defining the circulating current as

$$i_{\text{circ}} = \frac{1}{3} \left(i_{\text{arm}-ab} + i_{\text{arm}-bc} + i_{\text{arm}-ca} \right) \tag{83}$$

the following relationship for the converter arm currents is obtained:

$$\begin{bmatrix} i_{\text{arm}-ab} \\ i_{\text{arm}-bc} \\ i_{\text{arm}-ca} \end{bmatrix} = \frac{1}{3}\boldsymbol{E}_1 \begin{bmatrix} i_a \\ i_b \\ i_c \end{bmatrix} + \boldsymbol{U}_3 i_{\text{circ}} \tag{84}$$

with $\boldsymbol{U}_3 = [1\ 1\ 1]^T$.

Substituting (84) into (81), the instantaneous three-phase PWM converter voltages in the stationary *abc* frame can be expressed as follows:

$$\begin{bmatrix} v_{ab} \\ v_{bc} \\ v_{ca} \end{bmatrix} = \boldsymbol{E}_1 \left(L_{\text{eq}} \frac{d}{dt} \begin{bmatrix} i_a \\ i_b \\ i_c \end{bmatrix} + R_{\text{eq}} \begin{bmatrix} i_a \\ i_b \\ i_c \end{bmatrix} + \begin{bmatrix} e_a \\ e_b \\ e_c \end{bmatrix} \right) + \boldsymbol{U}_3 \left(L_{\text{arm}} \frac{di_{\text{circ}}}{dt} + R_{\text{arm}} i_{\text{circ}} \right) \tag{85}$$

where $R_{\text{eq}} = R + R_{\text{arm}}/3$ and $L_{\text{eq}} = L + L_{\text{arm}}/3$ represent the equivalent line resistance and inductance, respectively. Equation (85) governs the current dynamics.

REFERENCES

[1] G. Farivar, B. Hredzak, and V. G. Agelidis, "Reduced-capacitance thin-film h-bridge multilevel STATCOM control utilizing an analytic filtering scheme," *IEEE Trans. Ind. Electron.*, vol. 62, no. 10, pp. 6457–6468, Oct. 2015.

[2] G. Farivar, C. D. Townsend, B. Hredzak, J. Pou, and V. G. Agelidis, "Low-capacitance cascaded h-bridge multilevel StatCom," *IEEE Trans. Power Electron.*, vol. 32, no. 3, pp. 1744–1754, Mar. 2017.

[3] G. Farivar, C. D. Townsend, B. Hredzak, J. Pou, and V. G. Agelidis, "Passive reactor compensated cascaded h-bridge multilevel LC-StatCom," *IEEE Trans. Power Electron.*, vol. 32, no. 11, pp. 8338–8348, Nov. 2017.

[4] G. Farivar, C. Townsend, J. Pou, and B. Hredzak, "Low-capacitance StatCom with modular inductive filter," *IEEE Trans. Power Electron.*, vol. 34, no. 4, pp. 3192–3203, Apr. 2019.

[5] G. G. Farivar *et al.*, "Cascaded h-bridge low capacitance static compensator with modular switched capacitors," *IEEE Trans. Ind. Electron.*, vol. 68, no. 7, pp. 5944–5954, Jul. 2021.

[6] Y. Jeon *et al.*, "An enhanced static compensator with DC-link voltage shaping method," *IEEE Trans. Power Electron.*, vol. 35, no. 3, pp. 2488–2500, Mar. 2020.

[7] E. R. Rodriguez *et al.*, "Enhancing inductive operation of low-capacitance cascaded h-bridge StatComs using optimal third-harmonic circulating current," *IEEE Trans. Power Electron.*, vol. 36, no. 9, pp. 10788–10800, Sep. 2021.

[8] E. Rodriguez *et al.*, "Closed-loop analytic filtering scheme of capacitor voltage ripple in multilevel cascaded h-bridge converters," *IEEE Trans. Power Electron.*, vol. 35, no. 8, pp. 8819–8832, Aug. 2020.

[9] T. Isobe, L. Zhang, H. Tadano, J. A. Suul, and M. Molinas, "Control of DC-capacitor peak voltage in reduced capacitance single-phase STATCOM," in *Proc. IEEE 17th Workshop Control Model. Power Electron.*, Jun. 2016, pp. 1–8.

[10] Z. He, L. Zhang, T. Isobe, and H. Tadano, "Dynamic performance improvement of single-phase STATCOM with drastically reduced capacitance," in *Proc. IEEE 3rd Intern. Future Energy Electron. Conf. ECCE Asia*, Jun. 2017, pp. 1413–1418.

[11] E. R. Ramos, R. Leyva, G. G. Farivar, H. D. Tafti, C. D. Townsend, and J. Pou, "Incremental passivity control in multilevel cascaded h-bridge converters," *IEEE Trans. Power Electron.*, vol. 35, no. 8, pp. 8766–8778, Aug. 2020.

[12] X. Ge and F. Gao, "Flexible third harmonic voltage control of low capacitance cascaded h-bridge STATCOM," *IEEE Trans. Power Electron.*, vol. 33, no. 3, pp. 1884–1889, Mar. 2018.

[13] D. Niu *et al.*, "Cascaded packed u-cell STATCOM with low capacitance and its third harmonic control," in *Proc. IEEE Appl. Power Electron. Conf. Expo.*, Jun. 2020, pp. 529–534.

[14] G. Farivar, B. Hredzak, and V. G. Agelidis, "Decoupled control system for cascaded h-bridge multilevel converter based STATCOM," *IEEE Trans. Ind. Electron.*, vol. 63, no. 1, pp. 322–331, Jan. 2016.

[15] M. Hagiwara, R. Maeda, and H. Akagi, "Negative-sequence reactive-power control by a PWM STATCOM based on a modular multilevel cascade converter (MMCC-SDBC)," *IEEE Trans. Ind. Appl.*, vol. 48, no. 2, pp. 720–729, Mar. 2012.

[16] J. I. Leon, S. Vazquez, and L. G. Franquelo, "Multilevel converters: Control and modulation techniques for their operation and industrial applications," *Proc. IEEE*, vol. 105, no. 11, pp. 2066–2081, Nov. 2017.

[17] H. Akagi, S. Inoue, and T. Yoshii, "Control and performance of a transformerless cascade PWM STATCOM with star configuration," *IEEE Trans. Ind. Appl.*, vol. 43, no. 4, pp. 1041–1049, Jul./Aug. 2007.

[18] J. I. Y. Ota, Y. Shibano, and H. Akagi, "A phase-shifted PWM D-STATCOM using a modular multilevel cascade converter (SSBC)-part II: Zero-voltage-ride-through capability," *IEEE Trans. Ind. Appl.*, vol. 51, no. 1, pp. 289–296, Jan. 2015.

[19] J. Maciejowski, *Predictive Control: With Constraints*. Englewood Cliffs, NJ, USA: Prentice Hall, 2002.

[20] T. Geyer, *Model Predictive Control of High Power Converters and Industrial Drives*. Hoboken, NJ, USA: John Wiley & Sons, 2016.

[21] Y. Zhang, X. Wu, and X. Yuan, "A simplified branch and bound approach for model predictive control of multilevel cascaded h-bridge STATCOM," *IEEE Trans. Ind. Electron.*, vol. 64, no. 10, pp. 7634–7644, Oct. 2017.

[22] C. D. Townsend, T. J. Summers, J. Vodden, A. J. Watson, R. E. Betz, and J. C. Clare, "Optimization of switching losses and capacitor voltage ripple using model predictive control of a cascaded h-bridge multilevel StatCom," *IEEE Trans. Power Electron.*, vol. 28, no. 7, pp. 3077–3087, Jul. 2013.

[23] V. Spudic and T. Geyer, "Model predictive control based on optimized pulse patterns for modular multilevel converter STATCOM," *IEEE Trans. Ind. Appl.*, vol. 55, no. 6, pp. 6137–6149, Nov. 2019.

[24] M. Chai, N. B. Y. Gorla, and S. K. Panda, "Fault detection and localization for cascaded h-bridge multilevel converter with model predictive control," *IEEE Trans. Power Electron.*, vol. 35, no. 10, pp. 10109–10120, Oct. 2020.

[25] W. Brogan, *Modern Control Theory*. Englewood Cliffs, NJ, USA: Prentice Hall, 1991.

[26] B. O'Donoghue, G. Stathopoulos, and S. Boyd, "A splitting method for optimal control," *IEEE Trans. Control Syst. Technol.*, vol. 21, no. 6, pp. 2432–2442, Nov. 2013.

[27] J. Pou, S. Ceballos, G. Konstantinou, V. G. Agelidis, R. Picas, and J. Zaragoza, "Circulating current injection methods based on instantaneous information for the modular multilevel converter," *IEEE Trans. Ind. Electron.*, vol. 62, no. 2, pp. 777–788, Feb. 2015.

[28] M. Odavic, V. Biagini, P. Zanchetta, M. Sumner, and M. Degano, "One-sample-period-ahead predictive current control for high-performance active shunt power filters," *IET Power Electron.*, vol. 4, no. 4, pp. 414–423, Apr. 2011.

[29] P. Cortes, J. Rodriguez, P. Antoniewicz, and M. Kazmierkowski, "Direct power control of an AFE using predictive control," *IEEE Trans. Power Electron.*, vol. 23, no. 5, pp. 2516–2523, Sep. 2008.

[30] Y. Zhang, W. Xie, Z. Li, and Y. Zhang, "Model predictive direct power control of a PWM rectifier with duty cycle optimization," *IEEE Trans. Power Electron.*, vol. 28, no. 11, pp. 5343–5351, Nov. 2013.

[31] J. Rawlings and D. Mayne, *Model Predictive Control: Theory and Design*. Madison, WI, USA: Nob Hill Publishing, LLC., 2009.

[32] B. Kouvaritakis and M. Cannon, "Model predictive control: Classical, robust and stochastic," in *Advanced Textbooks in Control and Signal Processing*. London, U.K.: Springer, 2015.

[33] G. Farivar, H. Dehghani Tafti, C. D. Townsend, E. Rodriguez, and J. Pou, "Load adaptive cascaded h-bridge low capacitance StatCom with modular capacitors," in *Proc. IECON 45th Annu. Conf. IEEE Ind. Electron. Soc.*, vol. 1, 2019, pp. 3541–3546.

[34] B. Stellato, G. Banjac, P. Goulart, A. Bemporad, and S. Boyd, "OSQP: An operator splitting solver for quadratic programs," Nov. 2017, *arXiv:1711.08013*.

[35] G. Banjac, P. Goulart, B. Stellato, and S. Boyd, "Infeasibility detection in the alternating direction method of multipliers for convex optimization," *J. Optim. Theory Appl.*, vol. 183, no. 2, pp. 490–519, 2019.

Ezequiel Rodriguez (Student Member, IEEE) was born in Tarragona, Spain, in 1994. He received the bachelor's degree in electrical engineering and the master's degree in engineering and technology of electronic systems (with first class hons. for both B.S. and M.S. degrees) from Universitat Rovira i Virgili, Catalonia, Spain, in 2016 and 2017, respectively. He is currently working toward the Ph.D. degree with the School of Electrical and Electronic Engineering, Nanyang Technological University, Singapore.

His research interests include modeling and the control of power electronic converters, with an emphasis on modular multilevel cascade converters.

Ramon Leyva (Senior Member, IEEE) received the M.Sc. and Ph.D. degrees in telecommunication engineering from Universitat Politécnica de Catalunya, Barcelona, Spain, in 1992 and 2000, respectively.

He was a Visiting Professor with LAAS-CNRS, Toulouse, France, in 2002–2003, 2009, and 2010 and with the COPEC-University of Colorado at Boulder, Boulder, CO, USA, in 2012. He is currently an Associate Professor with the Departament d'Enginyeria en Electrónica, Eléctrica i Automática, Universitat Rovira i Virgili, Tarragona, Spain. He has coauthored more than 100 scientific publications, two books, and one patent and has been involved in more than 20 R&D projects. His research interests include nonlinear and robust control of power converters and renewable energy.

Dr. Leyva serves as reviewer for several IEEE and IET scientific publications.

Christopher D. Townsend (Member, IEEE) received the B.E. and Ph.D. degrees in electrical engineering from the University of Newcastle, Callaghan, Australia, in 2009 and 2013, respectively.

He spent three years with ABB Corporate Research, Västeras, Sweden, working on next-generation high-power converter technologies. Since then, he has held various Postdoctoral Research positions including with the University of New South Wales, Sydney, Australia, University of Newcastle, and Nanyang Technological University, Singapore. In 2019, he joined the Department of Electrical, Electronic and Computer Engineering, University of Western Australia, Perth, Australia, as a Senior Lecturer. He has authored more than 60 published technical papers and has been involved in several industrial projects and educational programs in the field of power electronics. His research interests include topologies and modulation strategies for multilevel converters applied in power systems, renewable energy integration, and electric vehicle applications.

Glen G. Farivar (Senior Member, IEEE) received the B.Sc. degree in electrical engineering from the Nooshirvani Institute of Technology, Babol, Iran, in 2008, the M.Sc degree in power electronics from the University of Tehran, Tehran, Iran, in 2011, and the Ph.D. degree in electrical engineering from the University of New South Wales, Sydney, Australia, in 2016.

He is currently a Postdoctoral Research Fellow with the Energy Research Institute, Nanyang Technological Institute (ERI@N), Singapore. His research interests include renewable energy systems, high power convertors, energy storage, FACTS devices, and hybrid electric vehicles.

Hossein Dehghani Tafti (Senior Member, IEEE) received the B.Sc. and M.Sc. degrees in electrical engineering and power system engineering from the Amirkabir University of Technology, Tehran, Iran, in 2009 and 2011, respectively, and the Ph.D. degree in electrical engineering from Nanyang Technological University, Singapore, in 2018.

He was a Research Fellow with Nanyang Technological University from 2018 to 2020, where he was working on the control of photovoltaic systems for grid support. From 2020 to 2021, he was a Senior Research Associate with the University of New South Wales, Sydney, Australia, where he worked on modeling and testing of commercial photovoltaic inverters. He is currently a Research Fellow with the Department of Electrical, Electronic and Computer Engineering, University of Western Australia, Perth, Australia. He was the Co-Editor of the book titled *Advanced Multilevel Converters and Applications in Grid Integration* (John Wiley, 2018). His research interest includes the grid-integration of renewable energy sources, in particular, photovoltaics and energy storage and design and control of multilevel power converters.

Josep Pou (Fellow, IEEE) received the B.S., M.S., and Ph.D. degrees in electrical engineering from the Technical University of Catalonia (UPC)-Barcelona Tech, Barcelona, Spain, in 1989, 1996, and 2002, respectively.

He joined the faculty of UPC as an Assistant Professor in 1990, where he became an Associate Professor in 1993. From 2013 to 2016, he was a Professor with the University of New South Wales (UNSW), Sydney, Australia. He is currently a Professor with the Nanyang Technological University (NTU), Singapore, where he is a Program Director of Power Electronics with the Energy Research Institute, NTU (ERI@N) and Codirector of the Rolls-Royce, NTU Corporate Lab, Singapore. From 2001 to 2002 and from 2005 to 2006, he was a Researcher with the Center for Power Electronics Systems, Virginia Tech, Blacksburg, VI, USA. From 2012 to 2013, he was a Visiting Professor with the Australian Energy Research Institute, UNSW, Sydney. He has authored more than 370 published technical papers and has been involved in several industrial projects and educational programs in the fields of power electronics and systems. His research interests include modulation and control of power converters, multilevel converters, renewable energy, energy storage, power quality, high voltage direct current transmission systems, and more-electrical aircraft and vessels.

Dr. Pou is currently an Associate Editor for the *IEEE Journal of Emerging and Selected Topics in Power Electronics*. He was a Co-Editor-in-Chief and Associate Editor for the IEEE TRANSACTIONS ON INDUSTRIAL ELECTRONICS. He is the recipient of the 2018 IEEE Bimal Bose Award for Industrial Electronics Applications in Energy Systems.